Title

Li$^+$ and Oxidant Addition To Control Ionic and Electronic Conduction in Ionic Liquid-Functionalized Conjugated Polymers

Journal

Chemistry of Materials, 33(16)

ISSN

0897-4756 1520-5002

Authors

Rawlings, Dakota
Lee, Dongwook
Kim, Jeongmin
et al.

Publication Date

2021-08-06

DOI

10.1021/acs.chemmater.1c01811

Peer reviewed

Li^+ and Oxidant Addition to Control Ionic and Electronic Conduction in Ionic Liquid Functionalized Conjugated Polymers

Dakota Rawlings,[1] Dongwook Lee,[2] Jeongmin Kim,[4] Ioan-Bogdan Magdau,[4] Gordon Pace,[1] Peter M. Richardson,[2] Elayne M. Thomas,[2] Scott P. O. Danielsen,[1] Sarah H. Tolbert,[5,6] Thomas F. Miller, III,[4] Ram Seshadri,[2,3] Rachel A. Segalman*[1,2]

[1]*Department of Chemical Engineering, University of California, Santa Barbara, Santa Barbara CA 93106, United States*

[2]*Materials Department, University of California, Santa Barbara, Santa Barbara CA 93106, United States*

[3]*Materials Research Laboratory, University of California, Santa Barbara, Santa Barbara CA 93106, United States*

[4]*Division of Chemistry and Chemical Engineering, California Institute of Technology, Pasadena, CA 91125, United States*

[5]*Department of Chemistry and Biochemistry, University of California Los Angeles, Los Angeles CA 90095, United States*

[6]*Department of Materials Science and Engineering, University of California Los Angeles, Los Angeles CA 90095, United States*

To whom correspondence should be addressed: segalman@ucsb.edu

Abstract

Conduction of ions and charge (electrons) often follow distinct materials design rules, presenting a significant challenge for the development of homogeneous materials that are good at both. The fundamental interactions that dictate ionic and electronic conduction in mixed conductors are still unclear. Here, we characterize the ionic and electronic conduction of a class of mixed polymeric conductors in which ionic liquid groups are tethered to an electron conducting conjugated polymer backbone. A model conjugated polymeric ionic liquid, poly{3-[6'-(N-methylimidazolium)hexyl]thiophene}BF_4^- (P3HT-IM), is synthesized and shown to have significant long range ordering. Chemical oxidation of the polymer results in a room temperature electronic conductivity of 10^{-2} S cm^{-1}. The polymer is also capable of dissolving Li^+ salt up to a concentration of r_{salt} = 1 [moles of salt]/[moles of monomer]. The polymer displays a monotonic increase in ionic conductivity with salt concentration, reaching a maximum room temperature ionic conductivity of 10^{-5} S cm^{-1} at the highest concentration of r_{salt} = 1. Notably, this is among the first studies to characterize both the ionic and electronic conductivity of an ionic liquid functionalized conjugated polymer upon the addition of oxidant and salt. All-atom molecular dynamics simulations indicate that the imidazolium side chains promote the formation of a percolated network of solvation sites at high salt concentrations, which facilitates ion transport. Pulsed-Field Gradient NMR diffusivity measurements and MD indicate a lithium transference number around 0.5, suggesting that the percolated solvation network promotes lithium transport in a way that is unique from many ion conducting systems. These results suggest that the addition of diffuse, ionic liquid-like groups to a conjugated polymer backbone serves as an effective design approach to facilitate simultaneous lithium-ion conduction and electronic conduction in the absence of solvent.

Introduction

Simultaneous ion and electron conduction is essential in all electrochemical devices and is particularly important for applications in energy storage and conversion.[1,2] Rational design of mixed conducting organic materials is challenging because ion and electron conducting materials follow different design rules.[3] Ion transport in polymers is generally correlated to segmental motion and is optimized in polar rubbery materials[1,4,5] while electron transport often relies on structural alignment in highly ordered polymeric systems.[2,3,6,7] Conjugated polymers are particularly promising in the field of mixed conductors because their electronic, ionic, and structural properties can be readily tuned through conventional synthetic design strategies.[3]

Ion conductivity in polymeric systems is dependent on the concentration and mobility of ions, which are related to the polarity and the segmental dynamics of the polymer.[6] For a given concentration of added salt, the mobile ion concentration depends on the extent of salt dissociation, which is affected by the local dielectric environment, the interactions between anions and cations, and interactions between the polymer and the ions.[4,6,8] Inclusion of highly polar functional groups and increasing the size and polarizability of ionic groups serves to increase the dielectric constant, weaken electrostatic interactions, and promote ion dissociation.[8–11] Additionally, the mobility of ions generally depends on the dynamics of the polymer system as solvation sites rearrange to create a conduction pathway.[12–14] For polymers above their glass transition temperature (T_g), the ionic mobility is often tied to the segmental dynamics of the polymer which is related to the distance from T_g.[12–14] However, ion dynamics are also affected by the nature of ion–ion and polymer–ion associations, where ion solvation sites and ion coordinating groups, which help ions dissociate, can decrease ion dynamics.[6,13]

Paradoxically, ionic aggregation can lead to higher ionic conductivity if aggregates percolate through the material.[12,15–17] Ion transport in many polymeric systems can be characterized by transport through a transient network of solvation sites,[18–21] where the mobility of ions is, in part, connected to the density and connectivity of solvation sites.[18] Local ion transport in aggregated domains is postulated to be higher in some systems due to the close proximity of solvation sites.[12,16,17,22,23] In this case, the ionic mobility is related to the extent to which aggregates form continuous domains through the material.[12,15–17]

In contrast to ion conduction, electron transport in semicrystalline conjugated polymers is often related to the degree of long-range order in the polymer and the degree of ionization.[7,24,25] Electronic conductivity is directly proportional to the carrier density and the electronic mobility.[7,24,26–28] The carrier density in conjugated polymers is commonly modulated via the introduction of a reductant (in the case of a n-type material) or an oxidant (in the case of a p-type material).[29–36] In the case of a p-type conjugated polymer, the polymer backbone undergoes electron exchange with the oxidant, resulting in the formation of an ion pair between the charge carrier on the polymer backbone and the ionized oxidant.[37–39] The mobility of the charge carriers depends on a number of structural and molecular factors. Generally, for semicrystalline conjugated polymers, crystalline domains are dispersed in an amorphous matrix.[40] Charge transport predominates in ordered regions, where co-facially stacked conjugated backbones have strong π-orbital interactions.[40] As a result, a general heuristic to increase electronic conductivity in semicrystalline conjugated polymers is to increase the degree of crystallinity and long-range order, however, the relationship between structural order and mobility is not well-defined.[25,28,41,42]

The incorporation of ion-conducting moieties into conjugated polymers serves as a route to provide conduction pathways for both ions and electrons. Optimization of ionic and electronic conduction in conjugated polymers requires a system with both highly ordered domains and polar domains with high

segmental mobility. Conjugated polymers with oligoethylene glycol side chains have shown both high ionic conductivity (≈10^{-4} S cm^{-1}) upon lithium salt addition and evidence of long-range order.[43–45] The addition of ionic moieties, such as sulfonate groups, to a conjugated polymer backbone promotes ion transport and ion injection in electrochemical devices.[45–52] These systems have also been used to improve the performance of bioelectronics due to their water solubility and ion conductivity.[2,50,51]

Ionic liquid moieties can be covalently tethered to a conjugated polymer backbone to enable ion conduction without the presence of solvent, which is particularly important for solvent-free electrochemical devices.[1,2,53] Mixed conducting conjugated materials are commonly employed as protective coatings and binders for cathode materials in batteries due to their easy processability and facile ion and electron transport in the presence of liquid electrolyte.[18,54–58] Increasing interest in solvent-free battery construction, however, has created a demand for materials that can conduct both ions and electrons without the presence of solvent.[18,19,56,57] Conjugated polymers with ionic liquid-like side chains, in which an ionic liquid group is covalently tethered to the polymer backbone, have considerable promise in the field of solvent-free mixed conduction.[59,60] Large, polarizable ionic side-chain moieties serve to weaken ionic associations and increase ion dynamics without the presence of solvent, while the conjugated backbone imparts electron conductivity.[61,62] Polythiophenes with imidazolium side chains have shown intrinsic ionic conductivity up to 10^{-4} S cm^{-1} in the neat state, while also showing evidence of significant long-range order in scattering studies.[60,63] While Ionic liquid functionalized conjugated polymers show potential as solvent-free mixed ion and electron conductors, to this point there have been few studies that investigate lithium-ion conduction in ionic liquid functionalized conjugated polymers. Furthermore, very few studies have characterized mixed conduction in conjugated systems upon simultaneous salt addition and oxidant addition.

Herein, the ionic and electronic transport properties of an ionic liquid functionalized conjugated polymer are investigated as a function of salt and oxidant addition. A semicrystalline polythiophene based system with imidazolium covalently tethered to the polymer backbone was developed as a model mixed conductor. The addition of both salt and oxidant to the polymer induces mobile ionic and electronic carriers without significantly disrupting the crystalline structure of the polymer, resulting in a simultaneous increase in the ionic and electronic conductivity. Surprisingly, the polymer solvates added salt up to a concentration of r_{salt} = 1 [mole of salt]/[mole of monomer] and displays a monotonic increase in ionic conductivity with salt concentration. MD simulations and PFG NMR diffusion measurements suggest that a percolating network of solvation sites forms at high concentrations, which facilitates lithium-ion conduction over a wide range of salt concentrations.

Results and Discussion

I. System Design

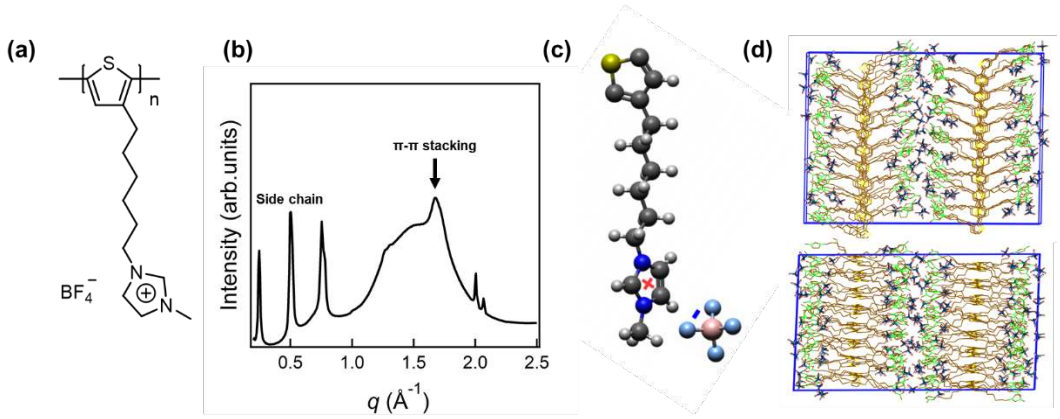

Figure 1: a) Schematic structure of the thiophene-based conjugated polymeric ionic liquid used in this study b) Azimuthally integrated GIWAXS profile for neat P3HT-IM. c) Illustration of the polymer model used in MD simulations. d) MD snapshot of the simulation box used for the crystalline polymer.

A semicrystalline polythiophene-based conjugated polymer with ionic side chains was developed as a model mixed ion and electron conductor (**Figure 1a**). Polythiophene serves as an ideal model conjugated polymer backbone because it belongs to a well-studied class of semicrystalline conjugated polymers with reasonable mobility and long-range order. To promote ion solvation, the polymer was synthesized with ionic liquid like groups covalently tethered to the polymer backbone. An ionic liquid like cationic imidazolium group was selected as the covalently tethered ion group because the diffuse, polarizable charge on the imidazolium fosters weak physical associations between ions. The structure and the transport properties of the polymer will also be influenced by the counterion to the pendent imidazolium group. Larger, polarizable counterions lead to weaker ionic associations and faster segmental dynamics due to the increase in free volume, however, the resulting increase in the side-chain volume fraction also disrupts long range ordering.[59] UV-vis spectroscopy reveals information about the degree of aggregation of the polymer as a function of counterion chemistry (**Figure S12**). Absorption peaks in UV-vis indicated a decrease in ordered structure as the ion size increased (**Figure S12).** Tetrafluoroborate (BF_4^-) was chosen as a model counterion for mixed conduction studies because the intermediate size imparts a low T_g (20°C) in the amorphous domain of the polymer (**Figure S13**) while still allowing for a high degree of long-range order in the crystalline domains. Complete counterion exchange from a bromine counterion to the desired counterion was confirmed using quantitative XPS analysis. The resulting polymer, Poly{3-[6'-(N-methylimidazolium)hexyl]thiophene}BF_4^- (P3HT-IM) is shown in **Figure 1a**. A high degree of semicrystalline order is evident in the grazing incidence wide angle X-ray scattering (GIWAXS) patterns for drop cast films of P3HT-IM shown in **Figure 1b.** A series of peaks starting with a first order peak at q = 0.247 $Å^{-1}$ and higher order peaks at integer multiples indicate a lamellar side chain stacking structure, while a peak at q=1.674 $Å^{-1}$ corresponds to π-π stacking.[18,19,63–65]

II. Inducing ionic and electronic carriers

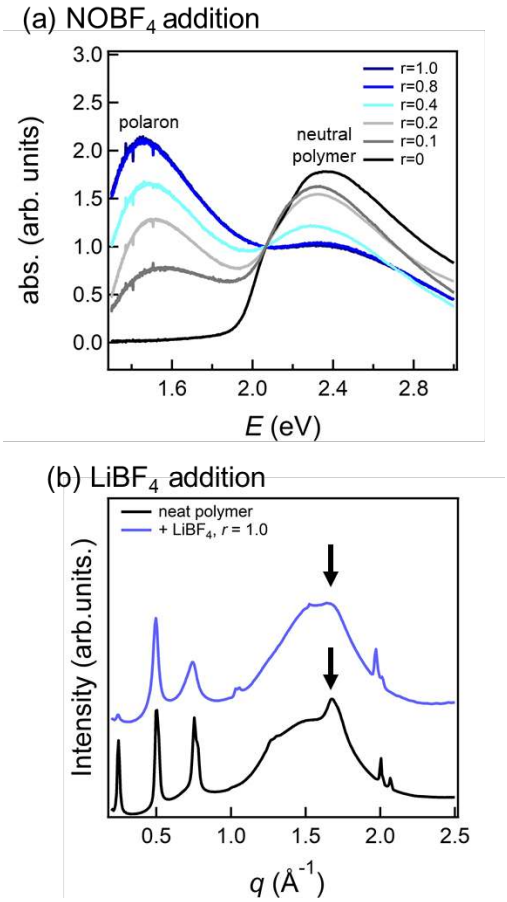

Figure 2: a) UV-vis spectra as a function of $NOBF_6$ oxidant addition. b) Integrated GIWAXS patterns for neat P3HT-IM and P3HT-IM with added $LiBF_4$ (r_{salt} = 1.0)

The addition of $LiBF_4$ and $NOBF_4$ to P3HT-IM introduces ionic and electronic carriers, respectively, without significantly perturbing the long-range ordering. To induce mobile electronic carriers and increase the electrical conductivity, an oxidant was added to P3HT-IM in solution state before casting. Nitrosonium tetrafluoroborate ($NOBF_4$) serves as a model oxidant because upon oxidizing the polymer, NO is released as a gas. This leaves BF_4^- as the counterion to the electronic carrier, which ensures that all mobile anions in the sample are the same. Optical spectra shown in **Figure 2a** have signatures which demonstrate that the polymer is ionized by $NOBF_4$. The appearance of a broad absorption below 1.9 eV as NOBF4 is added to the polymer, corresponds to polaronic charge carriers in the film. This is accompanied by the loss of the spectral signature for the neutral polymer, centered around 2.3 eV. These optical signatures indicate that mobile electronic charge carriers are induced in the P3HT-IM sample upon the addition of $NOBF_4$ oxidant.[66,67]

Grazing-incidence wide-angle X-ray scattering (GIWAXS) studies indicate that the addition of lithium salt to the polymer causes some disruption to the crystallinity, however, the polymer still retains crystalline order. (**Figure 2b**). Dropcast samples of P3HT-IM show scattering features indicative of crystalline ordering. Since the samples are relatively thick (≈ 5 μm), no substrate-induced texturing is observed. Small peaks at q = 1 Å^{-1} and q = 2 Å^{-1} appear in both the neat polymer and the polymer with added salt, likely corresponding to a crystalline impurity in the sample. For the neat polymer sample, a series of peaks at low q correspond to side-chain stacking, with a first order reflection at q = 0.247 Å^{-1} (d

= 2.54 nm), and two higher order peaks at integer multiples of the first peak (q = 0.504 Å^{-1} and q = 0.754 Å^{-1}). This is indicative of a lamellar structure with domains comprised of the π-stacked conjugated backbone and the side chains.[59,60] Note that the charge side groups are nanophase-separated from the thiophene backbone, and confined to a lamellar domain. As a result, it is likely that added salt will partition into the more polar side-chain stacking region. A peak at q = 1.674 Å^{-1} (indicated by the arrow in **Figure 2b**) corresponds to π-stacking of the thiophene backbone,[59,60] while the amorphous halo around q = 1.5 Å^{-1} likely corresponds to disordered π-stacks in the amorphous regions of the film. Ionic aggregation in polymers with ionic liquid side chains often results in a broad reflection in this region as well.[11,15,16] Lithium tetrafluoroborate ($LiBF_4$) salt was added as the mobile ionic component, and scattering patterns for the polymer with added salt are shown in **Figure 2b**. For samples with the highest concentration of added salt (r_{salt} = 1.0), both π-stacking peaks and side-chain stacking peaks are still present. Lamellar stacking peaks appear at (q = 0.240 Å^{-1}, q = 0.497 Å^{-1} and q = 0.741 Å^{-1}), indicating only a small increase in the alky stacking distance. As expected, some peak broadening is observed as the added salt introduces defects/disorder to the crystalline structure. A decrease in intensity of the first order side chain stacking peak is also observed, however, this is likely not an indication of the degree of crystallinity because the 2nd and 3rd order peak still have similar intensities when compared to the neat polymer. Rather, this is likely an indication that the drop cast film is not flat, and the tilted surface results in a decrease in low angle scattering. While the addition of salt expectedly results in a decrease in crystallinity, these scattering studies indicate that samples with added salt retain semicrystalline order.

III. ***Mixed ionic and electronic conductivity***

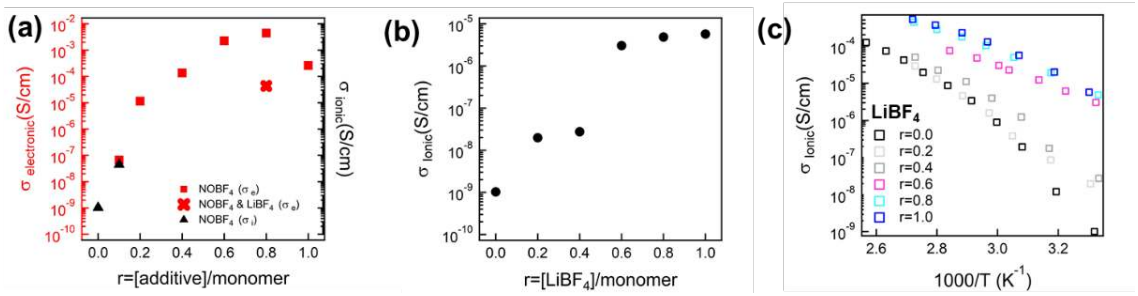

Figure 3: a) Electronic conductivity as a function of $NOBF_4$ oxidant addition. The electronic conductivity of the polymer with both $NOBF_4$ and $LiBF_4$ is indicated by the red x. b) Ionic conductivity as a function of lithium salt addition at room temperature c) Ionic conductivity as a function of temperature for P3HT-IM with different added salt concentrations, where r is the ratio of the moles of salt to the moles of monomer.

The electronic conductivity and the ionic conductivity of P3HT-IM can be simultaneously tuned through the addition of salt and oxidant. Upon oxidation of the thiophene backbone via electron exchange with NO, both ionic charge carriers (mobile BF_4^- counterions) and electronic charge carriers are present in the polymer. To measure the electronic conductivity, DC conductivity measurements were performed on the sample (see **Figure S15** for more details). The electronic conductivity ($\sigma_{electronic}$) of the polymer is plotted as a function of oxidant concentration in **Figure 3a.** As expected, the electronic conductivity increases with oxidant concentration up to $r_{oxidant}$ = 0.6 ($r_{oxidant}$ = [$NOBF_4$]/[monomer]) as the electronic carrier concentration increases. $\sigma_{electronic}$ reaches a maximum of 4.45 x 10^{-3} S/cm at $r_{oxidant}$ = 0.8. This electronic conductivity is lower than that of analogous oxidized alkyl substituted conjugated polymers in literature such as vapor doped P3HT thin films ($\sigma_{electronic} \approx 10^1$ S/cm).[68] However, conjugated polymers with ionic side chains often show lower conductivities, likely because ionic groups can perturb crystalline ordering. For example, the conductivity of conjugated polymers such as PEDOT,[69] P3HT,[70] and

PCPDTBT[51] with sulfonate side chains has been found to be in the range of 10^{-4} to 10^{-1} S/cm after oxidant addition. While this conductivity is low for many applications in organic electronic devices, it is significant for applications in battery electrode binder materials. Electrochemically doped conjugated polymers with electronic conductivities in the range of 10^{-3} to 10^{-1} S/cm have been shown to dramatically increase the performance of NCA electrodes when employed as battery binders.[18] As the oxidant concentration is increased beyond $r_{oxidant} = 0.8$, $\sigma_{electronic}$ decreases. This behavior is observed in many conjugated polymer systems[26] and is attributed to "over charging" of the thiophene backbone at high ionization levels, in which the HOMO level becomes empty, preventing charge hopping along the backbone.[26,71,72] To show that both salt and oxidant can be added to the polymer to independently tune the ionic and electronic conductivity, $LiBF_4$ and $NOBF_4$ were added simultaneously, both at a concentration of $r = 0.8$ (r = [additive]/[monomer]). As suggested by the peak broadening in the GIWAXS (**Figure 2b**), $LiBF_4$ does affect the crystalline order of the polymer at high concentrations, which in turn affects the electronic conduction pathways in the polymer. Peak broadening is observed in samples with added $NOBF_4$, and to an even greater extent in samples with both $NOBF_4$ and $LiBF_4$ (**Figure S17**), however, all samples show clear π-π and alkyl stacking. This accounts for the decrease in electronic conductivity for the polymer with both $NOBF_4$ and $LiBF_4$ when compared to the electrical conductivity with only $NOBF_4$ added (**Figure 3a**). To understand the dynamics of ions in the polymer, electrochemical impedance spectroscopy (EIS) was performed on the bulk polymer with added oxidant. An equivalent circuit was fit to the Nyquist plot which accounts for the ionic resistance, the electronic resistance, and the contact resistance (see **Figure S14** for more details on Nyquist plot fitting). The ionic conductivity of P3HT-IM, shown in black in **Figure 3a**, increases with oxidant addition because the oxidant introduces mobile anions in the polymer which are associated with holes on the thiophene backbone. Since the electronic signal overwhelms the ionic signal in the Nyquist plot at higher oxidation levels, the ionic conductivity was not measured beyond an oxidant concentration of $r_{oxidant} = 0.1$.

P3HT-IM is capable of solvating and transporting $LiBF_4$ over a wide range of salt concentrations. The lack of diffraction peaks specific to crystalline $LiBF_4$ in GIWAXS patterns for P3HT-IM with added salt (**Figure 2b**) suggests that salt does not precipitate out of the polymer, and thus the salt is well solvated by the polymer even at high concentrations (r_{salt}=1.0). At this concentration, the sample is roughly 22% salt by mass, which is comparable to many lithium conducting systems in the literature. By comparison, poly(ethyleneoxide) (PEO) generally shows salt precipitation beyond a salt concentration of r_{salt}=0.2 (≈62 % salt by mass for LiTFSI).[6,73,74] Ionic liquids such as EMIM TFSI can solvate salt beyond concentrations of r_{salt}=0.4 (≈50% salt for LiTFSI in EMIM TFSI).[75–78] Since the addition of salt alone, without NOBF4 addition, does not introduce a significant number of electronic charge carriers to the polymer, only ionic charge carriers are present in significant concentrations following $LiBF_4$ addition. EIS was used to understand ion transport in the bulk polymer with added salt (see **Figure S14** for more details on EIS measurements and analysis). Surprisingly, the ionic conductivity of the polymer shows a monotonic increase up to the highest salt concentration of $r_{salt} = 1.0$ (**Figure 3b**). By contrast, most polymeric ion conductors with ion coordinating groups are incapable of solvating salt at concentrations higher than $r_{salt} = 0.5$,[6,12,13,15,16,79–81] and often show a maximum in conductivity at intermediate salt concentrations (generally $r_{salt} = 0.1$ to $r_{salt} = 0.2$) due to salt aggregation and physical cross-linking.[4,79,82,83] P3HT-IM displays ionic conductivities between 10^{-8} to 10^{-6} S/cm depending on salt addition. These ionic conductivity values are similar to that of many polymeric ionic liquids with added lithium salt at lower concentrations ($r_{salt} = 0.02$ to $r_{salt} = 0.2$).[12] It is also worth noting the stark jump in conductivity observed at $r_{salt} = 0.6$. This suggests that there is a structural/mechanistic change in the system beyond this salt concentration that aids ion transport, the mechanism of which can be investigated in detail via diffusion measurements and MD simulations.

IV. MD simulation

Molecular dynamics (MD) simulations were performed to provide mechanistic insights on ion solvation and transport in both crystalline and amorphous phases of P3HT-IM (**Figure 1c**). For simulations of the crystalline domains of the polymer, the crystalline structure of the polymer remained stable as a stacked configuration characteristic of most thiophene based polymers, in which clear π-π stacking and lamellar alkyl spacing were observed (**Figure 1d**). This agrees with the structural features observed experimentally via GIWAXS (**Figure 2**). Addition of salt to the simulation enables a detailed characterization of the solvation environment for both Li^+ and BF_4^- in the polymer (see **Figure S6, S7** and our previous work[20] for detailed analysis on Li^+ ion solvation environment characterization)**.** For MD simulations of the crystalline polymer, both Li^+ and BF_4^- ions segregate in the confined lamellar regions formed by the charged side chains (**Figure S1**). At low salt concentrations, a fraction of Li^+ in the system is solvated (in part) by thiophene while most ions are coordinated by three BF_4^- counterions. At high salt concentrations Li^+ ions are almost exclusively coordinated by four BF_4^- counterions (**Figure 4b** and **4d**). A similar analysis for BF_4^- reveals that BF_4^- is solvated by the imidazolium and Li^+ ions. As the salt concentration is increased, the imidazolium contributes less to BF_4^- solvation, and the counterion becomes coordinated by up to two lithium ions in its first solvation shell (**Figure 4a and 4c**). This suggests that the mobility of BF_4 ions upon adding $LiBF_4$ salt may not be significantly affected by the presence of tethered imidazolium groups, since the BF_4 ions become increasingly detached from the imidazolium as the salt concentration increases. Overall, the observed shift in the nature of Li^+ and BF_4^- solvation with salt concentration indicates that the solvation structures are becoming more independent from the polymer backbone, where mobile ions are mainly interacting with other mobile ions of opposite charge.

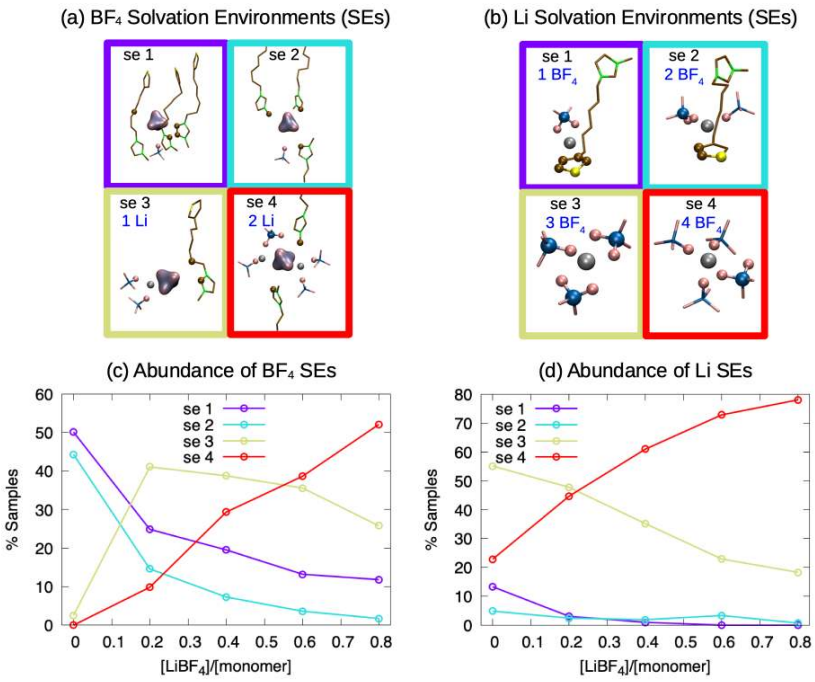

Figure 4: MD simulation results for the ion solvation environment in crystalline P3HT-IM polymers at different salt concentrations at 300 K (detailed analysis is reported in the SI) a) Snapshots of representative BF_4^- solvation environments in P3HT-IM and c) their abundance as a function of salt

concentration b) Snapshots of representative Li^+ solvation environments in P3HT-IM and d) their abundance as a function of salt concentration

Ion-solvation structures in P3HT-IM become more interconnected as the salt concentration is increased. Ion transport in the polymer network is, in part, dependent on the distance between solvation sites.[18,20,21] Accordingly, the density and connectivity of solvation environments in the polymer influences the ion dynamics. The spatial distribution of Li^+ solvation in MD simulations is illustrated in **Figure 5a and 5b** for the amorphous polymer and **Figure S2** for the crystalline polymer. At low salt concentrations, Li^+ solvation sites are dispersed in the polymer matrix and are characterized by localized ion-pairs between Li^+ and BF_4^-. At high salt concentrations, however, the ion solvation sites form transient interconnected networks, percolating throughout the simulation box (**Figure 5c** and see SI for the details). In the amorphous phase, pendent imidazolium side chains stabilize a percolated solvation network throughout the amorphous domain. In the crystalline P3HT-IM polymer, these percolating solvation networks are planar and confined to the inter sidechain region, which is delimited by high dielectric sheets formed by the charged imidazolium groups (**Figure S1**). The segregation of ions in these confined regions is more energetically favorable than a uniform distribution throughout the lattice which would destabilize the π-π stacking. This mechanism is supported by GIWAXS experiments which found that π-π stacking remains intact upon the addition of salt even at the highest concentration, indicating that the salt is predominantly located in the inter-side-chain stacking region. These percolating structures also likely contribute to the ability of the polymer to solvate $LiBF_4$ salt at higher concentrations when compared to many common ion conducting polymers.

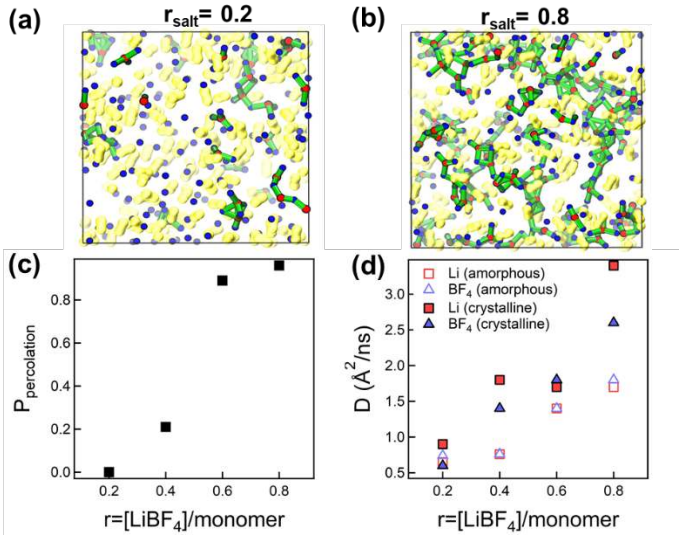

Figure 5: Simulation results for ion solvation and transport in the amorphous P3HT-IM polymer at 400 K. a) Dispersed localized ion pairs of Li^+ and BF_4^- at low salt concentration (r_{salt} = 0.2) b) Percolating network of Li^+ and BF_4^- at high salt concentration (r_{salt} = 0.8). c) Probability, P_{perc}, that the largest ionic network in the amorphous P3HT-IM polymer percolates the simulation box at several salt concentrations. d) Calculated diffusion coefficients for Li^+ and BF_4^- as a function of salt concentration in both the amorphous (open symbols) and crystalline polymer (solid symbols) at 400K. The color code for a) and b) is as follows: Red spheres represent Li^+; blue spheres represent BF_4^-; and yellow surfaces represent imidazolium groups; green lines connect neighboring Li^+ and BF_4^- within 4 Å. Calculated ion concentrations and total ion and monomer counts for each simulation can be found in **Table S3**

The increased ion network interconnectivity at high salt concentrations leads to faster ion dynamics. Long MD trajectories (50 to 100 ns) were used to monitor the dynamics of ions in the polymer and understand how the change in the ion network connectivity affects ion transport. The average contact duration between Li^+ and BF_4^- is plotted in **Figure S2f** for the amorphous polymer and **Figure S2c** for the crystalline polymer**.** This reveals that the average contact duration between ions is shorter at higher salt concentrations, which suggests that the formation of a percolated solvation network decreases the time scale of ion-ion interaction and thereby increases ion mobility. In this system, ion transport can be characterized by a hopping motion between solvation sites in a transient network. The increased proximity and connectivity of the solvation network at high salt concentrations aids ion hopping dynamics, leading to a lower average contact duration.[23,84] This supports the monotonic increase in ion conductivity observed in experimental impedance measurements (**Figure 3**). The discontinuous change in conductivity observed in the experiment at around r_{salt} = 0.6 could be understood as a transition into the percolating regime. **Figure 5c** shows the calculated probability, P_{perc}, that an ionic network will percolate the entire simulation box at various salt concentrations. These calculations reveal a jump in P_{perc} between r_{salt}=0.4 and r_{salt}=0.6, which corresponds with the jump in the ionic conductivity measured via impedance spectroscopy (**Figure 3b**), indicating that the formation of percolated solvation networks increases ion transport.

Experimentally measured ion dynamics align closely with ion dynamics in MD simulations. To further investigate ion transport, mean squared displacements (MSD) for both Li^+ and BF_4^- were calculated in the MD simulation to estimate the diffusivity of different ion species over a range of salt concentrations (**Figure S3**). A jump in the diffusion constants for both ions is observed at intermediate salt concentrations for both the crystalline and amorphous simulations (**Figure 5d**), in agreement with the experimentally measured jump in conductivity shown in **Figure 3**. Furthermore, the calculated diffusivities of Li^+ and BF_4^- are similar over the entire range of salt concentrations (**Tables S1 and S2)** with a transference number of approximately 0.5. To further corroborate the ion dynamics observed in MD simulations with the experimental polymer system, pulsed-field-gradient (PFG) NMR was used to measure the self-diffusion coefficients of ^{7}Li and ^{19}F in P3HT-IM upon salt addition at a concentration of r_{salt} = 1.0. The measured self-diffusion coefficients were .0145 Å^2/ns for ^{7}Li and .0101 Å^2/ns for ^{19}F at 353K. As detailed in the **Supporting Information**, this results in a lithium transference of t_{Li} = 0.59, which is in close agreement with the transference numbers found in MD simulations (**Table S1 and S2**). In contrast, lithium transference numbers in polymers with ion coordinating groups, such as PEO, PAN, and PVA, generally display transference numbers between 0.1 to 0.33[6]. This suggests that the ion transport mechanism in P3HT-IM deviates from that of standard ion-conducting polymers and further supports the formation of a percolating ionic network as the main mechanism for ion transport. The agreement between PFG NMR, conductivity, and MD simulations on the trend in ion diffusivity and transference number in P3HT-IM supports the ion transport mechanism observed in simulations.

Conclusion

The ionic and electronic conductivity of Poly{3-[6'-(N-methylimidazolium)hexyl]thiophene}BF_4^- (P3HT-IM) are dependent on a range of inter-related structural and chemical factors. In the neat state, the polymer shows evidence of crystalline order with scattering features indicative of π–π stacking and side-chain stacking. The addition of salt induces some structural disorder; however, the polymer still shows scattering features indicative of crystalline ordering, even at high concentrations (r_{salt} = 1). This long-range ordering facilitates electron transport, and upon oxidant addition, the polymer displays electronic conductivity up to 10^{-2} S cm^{-1}. P3HT-IM is also capable of solvating $LiBF_4$ salt up to a concentration of r_{salt} = 1, as evidenced by the lack of peaks for the crystalline salt in scattering studies. Surprisingly, the

polymer displays a monotonic increase in ionic conductivity up to this concentration. This work provides new insight into both the electronic and ionic transport properties of a solvent-free conjugated polymeric ionic liquid as a function of oxidant and salt addition. MD simulations indicate that ion solvation and conduction at high salt concentrations is enabled by the formation of a percolated network of solvation sites at high salt concentrations, which facilitates ion transport. Furthermore, experimental PFG NMR diffusivity measurements and MD calculations indicate a lithium transference number of approximately 0.5, suggesting that the percolated solvation network promotes lithium transport in a way that is unique from many ion conducting systems. These results suggest that the addition of diffuse ionic liquid like groups to a conjugated polymer backbone serves as an effective design approach to facilitate simultaneous lithium-ion conduction and electronic conduction in the absence of solvent, which has significant utility in the field of cathode binders and cathode coatings for solvent-free lithium-ion batteries.

Experimental Methods

I. Molecular dynamics

All-atom molecular dynamics simulations were carried out to provide molecular-level mechanistic insights into ion solvation and ion transport. Simulations for P3HT polymers with charged imidazolium side chains were carried out in both crystalline and amorphous phases. Initial configurations of crystalline polymers were generated by stacking 16 straight polymer chains into two separate adjacent stackings (8x2 grid), where each chain consisted of 10 monomers. A BF_4^- counterion was added in the proximity of each imidazolium$^+$ moiety to balance the positive charge. Additionally, an equal number of Li^+ and BF_4^- ions were added in random positions in the simulation box to study the effects of salt concentration. The Li-free polymer (r = 0) was equilibrated for 5 ns. The additional salt was added in gradually, 32 ion pairs at a time (r = 0.2), and at every stage the simulation was equilibrated for an additional 1 ns. Amorphous polymers at each salt concentration were prepared by annealing the crystalline polymers at a higher temperature of 600 K for at least 2 ns, followed by an additional 10 ns equilibration at 400 K.

The OPLS force field,[85] a non-polarizable and all-atom model, was used to describe the potential energy functions of all molecules. Interactions between atoms were described using both electrostatic and Lennard-Jones (LJ) interactions. The cross terms of LJ interaction were obtained using the geometric mixing rule. Intramolecular interactions were described using harmonic potential energy functions for bonds and angles, and the sum of cosine functions for dihedral and improper angles. Bonding and non-bonding coefficients were obtained using the online generator LibParGen.[86] To incorporate the effects of polarizability for ionic species, all atomic charges were multiplied by a constant scalar (0.7) as previously suggested in the MD literature.[87,88] All simulations were conducted using the LAMMPS simulation package.[89]

In all cases during both equilibration and production runs, the MD trajectories were integrated using the velocity-Verlet algorithm with a timestep of 1 fs. Both LJ and Coulomb interactions were cut at 12 Å, and particle-particle particle-mesh Ewald summation[90] was used to compute Coulomb interactions beyond the cutoff distance. Periodic boundary conditions (PBC) were applied for both crystalline and amorphous polymers. The Nosé-Hoover thermostat (100 fs relaxation) and the Nosé-Hoover barostat (1000 fs relaxation) were applied in all simulations to control the temperature (300 K or 400 K) and the pressure (1 atm). All transport properties reported here were averaged using simulation trajectories over at least 80 ns after at least 20 ns long equilibration. Charge mean-squared displacement calculations are detailed in the SI.

To quantify the percolation transition of the ionic network as a function of salt concentration, we construct a graph whose nodes are Li ions and B atoms of BF_4 ions. Edges between the nodes are defined if the distance between Li and B is less than 4 Å. We use NetworkX (https://networkx.org) to find the largest cluster in the graph. We define the largest cluster to percolate the simulation box if the longest distance between two Li ions in the cluster is larger than the simulation box size. In this calculation, all the Li ions in the cluster are in the primitive simulation cell, and the longest distance is calculated without periodic boundary conditions applied. Then, the probability of forming a percolating ionic network, P_{perc}, is calculated: $P_{perc} = \langle p \rangle$, where $p = 1$ if the largest cluster percolates the simulation box, or 0 otherwise.

Solvation environments (SE) of the Li^+ and BF_4^- were studied in the crystalline phase, using the Solvation Environment Classification (SEC) machine learning approach published in our recent work.[20] The molecular environments visited by the ions were characterized using atom-specific cumulative distribution functions (CDFs) calculated with respect to the center of the ion (Li atom for the cation and B atom for the anion). These CDFs (averaged over 10 ps) were concatenated into feature vectors which were embedded in two-dimensional latent space and classified into specific SEs based on the similarity of molecular environments using SEC. Multiple short sample trajectories were used to allow for sufficient sampling of the SEs. The same number of feature vectors ($N_{traj} \times N_{ions} = 9600$) was obtained at each salt concentration by adjusting the number of sampling trajectories to compensate for the varying number of ions. The characterization of SEs resulting from the classification was obtained by inspecting average CDFs, ion binding energy (the non-bonding energy contribution of the force field) and characteristic atomic configurations sampled from each environment.

II. Synthetic methods

Poly[3-(6'-bromohexyl)thiophene] (P3BrHT) was synthesized according to previous literature.[61,62] An oven-dried Schlenk flask containing 2,5 dibromo-3-(6-bromohexyl)thiophene was placed under vacuum for 2 hours. Dry, degassed THF was added via syringe and the mixture was sparged with Nitrogen. Isopropylmagnesium chloride was added dropwise and the mixture was stirred for 1 h at ambient temperature under Nitrogen. The desired amount of Ni(dppp)Cl2 was added via syringe. The polymerization was stirred for 1 h at 60°C and quenched by rapid addition of 5 N HCl, and precipitated into methanol. The polymer was purified by washing in a Soxhlet apparatus with methanol, ethyl acetate, and hexanes before extraction with THF. The product was concentrated under vacuum, redissolved in a small amount of THF, and precipitated into rapidly stirring, cold methanol. The isolated product, a purple solid, was dried at 65◦C under vacuum to remove any remaining solvent.

Poly{3-[6'-(N-methylimidazolium)hexyl]thiophene} was post-functionalized through an amine quaternization reaction. The polymer was first dissolved in THF. 1 methylimidazole (10 eq.) was added to the solution in ambient conditions. The solution was then stirred for 24 h under reflux. After 12 h, some polymer precipitate was observed int eh flask. A small amount of methanol was added to fully dissolve the resulting polymer and the solution was stirred for an additional 24 hours to help achieve quantitative conversion. The polymers were then dialyzed using 10 kDa cutoff dialysis membranes against a mixture of methanol and THF, with the dialysate replaced every 12 h. The resulting polymer was then mixed with 10 molar equivalents of $LiBF_4$ and stirred at 50°C in methanol and acetonitrile followed by dialysis for 48h in a 50:50 mixture of methanol and acetonitrile and an additional 48h dialysis in acetonitrile. The isolated product was obtained as a red solid after removing the solvent under reduced pressure. Complete counterion exchange from a bromine counterion to the desired counterion was confirmed using quantitative XPS analysis, following procedures from our previous work.[91]

V. Pulsed Field Gradient NMR measurements

Pulsed Field Gradient (PFG) NMR measures the self-diffusion coefficients of any NMR active nuclei. 7Li and 19F are both NMR active, and correlate to the cation and anion in our system, respectively. Operating under the assumptions of Dilute Solution Theory, the lithium transference number (t_{Li+}) can be calculated, as shown in the following equation: $t_+ = \frac{D_+}{D_+ + D_-}$

The PFG NMR sample was prepared at a molar salt concentration of r=1.0 in the same manner as described for the AC Impendence samples. Here, dropcasting was performed into a quartz trough that facilitated approximately 100 mg of material to be loaded into the center of the standard 5mm NMR tube. All sample preparation was done in a nitrogen glovebox, and the NMR tubes were sealed before removal from the glovebox to maintain an oxygen and water free environment during measurement.

Measurements were performed on a 300 MHz Bruker Avance III super-wide-bore spectrometer with a Bruker DIFF50 diffusion probe with replaceable 10 mm radio- frequency (RF) inserts for 7Li and 19F. Due to signal noise and slow diffusion times at room temperature, measurements were performed at 80 C on both ^{19}F and ^{7}Li nuclei. A stimulated echo pulse sequence was used to conserve signal from relatively short T2 values, and the attenuation of the intensity (I) was fit to equation: $I(G) = I(0)\exp\left[-G^2 D\,\gamma^2\delta^2\left(\Delta - \frac{\delta}{3}\right)\right]$

Where G is the magnetic field gradient strength, $I(0)$ is the intensity of the magnetization when G=0, γ is the gyromagnetic ratio, δ is the gradient pulse duration, Δ is the interval between gradient pulses, and D is the self-diffusion coefficient.

VI. Impedance Measurements for ionic conductivity

P3HT-IM was prepared by dissolving the polymer in acetonitrile and casting onto a ¼ inch indium tin oxide (ITO) substrate with a circular well in a 150 μm Kapton spacer. $LiBF_4$ salt and $NOBF_4$ were added to the acetonitrile at the specified concentrations prior to casting. The samples were dried under high vac for 24 hours and enclosed with a second ITO substrate. A biologic SP-200 potentiostat was used to perform impedance measurements.

To distinguish the ionic and electronic contributions to the signal, an equivalent circuit was fit to the Nyquist plot which accounts for the ionic resistance, the electronic resistance, and the contact resistance. This was used to determine the ionic conductivity (for electronic conductivity measurements, see section VII). An equivalent circuit consisting of constant phase elements and resistors was utilized. A mixed conducting model circuit was used with a purely resistive component in parallel with an ionic component (a resistor and a constant phase element in series) to account for the electronic and ionic conduction of P3HT-IM. Since the electronic resistance is relatively high for samples with only $LiBF_4$ added, an equivalent circuit without R_e could also be appropriate here. However, we found that the equivalent circuit in **Figure S14** provided a better fit for all data. Furthermore, a pure ion conducting equivalent circuit without the R_e component should give nearly equivalent ionic resistance values compared to the mixed conducting circuit with R_e when the R_e is significantly higher than R_i. From the model circuit in **Figure S14**, the resistance $R_{int\#1}$ at the intercept of the first semicircle with the Z' axis for each Nyquist plot can roughly be expressed as $\frac{1}{R_{int\#1}} = \frac{1}{R_i} + \frac{1}{R_e}$. When the electronic resistance is significantly higher than R_i, the $\frac{1}{R_e}$ term is negligible, and thus the intercept of the first semicircle accurately represents the ionic resistance.

VII. Electronic conductivity measurements (DC)

P3HT-IM was prepared for electronic conductivity measurements by dissolving the polymer in acetonitrile and casting onto a ¼ inch indium tin oxide (ITO) substrate with a circular well in a 150 μm Kapton spacer. $LiBF_4$ salt and $NOBF_4$ were added to the acetonitrile at the specified concentrations prior to casting. The samples were dried under high vac for 24 hours and enclosed with a second ITO substrate. A biologic SP-200 potentiostat was used to perform DC conductivity measurements. Here, the voltage was increased in a stepwise manner. The voltage was held for 2.5 minutes at each voltage step to allow the ionic current to relax. This ensured that the measured current was solely from electronic conduction. The plateau current at each voltage value was then plotted vs. voltage (as shown in **Figure S15e**), the slope of the line was used to determine the electronic resistance.

Acknowledgements

We gratefully acknowledge the Center for Synthetic Control Across Length-Scales for Advancing Rechargeable (SCALAR), an Energy Frontier Research Center funded by the U. S. Department of Energy, Office of Science, Basic Energy Sciences under Award #DE-SC0019381, for support of device fabrication, simulations, and materials characterization. D.R. gratefully acknowledges support from the Department of Energy Office of Basic Energy Sciences (DE-SC0016390) for polymer synthesis. The research reported here made use of shared facilities of the National Science Foundation Materials Research Science and Engineering Center (MRSEC) at UC Santa Barbara (NSF DMR 1720256), which is a member of the Materials Research Facilities Network (www.mrfn.org). This research used X-ray scattering resources (NSLS-II, beamline 11-BM, Brookhaven National Laboratory) of the National Synchrotron Light Source II, a U.S. Department of Energy (DOE) Office of Science User Facility operated for the DOE Office of Science by Brookhaven National Laboratory under Contract No. DE-SC0012704. G.T.P gratefully acknowledges support from the National Science Foundation Graduate Research Fellowship Program under Grant No. 1650114. Any opinions, findings, and conclusions or recommendations expressed in this material are those of the author(s) and do not necessarily reflect the views of the National Science Foundation.

Associated Content

The supporting Information is available free of charge on the ACS Publications website at http://pubs.acs.org

> The supporting information includes detailed information on MD simulations for both the crystalline and amorphous domains of the polymer, synthetic details for the conjugated polymer, UV-vis spectrum of the polymer with various counterions, glass transition temperature data as a function of salt and oxidant addition, details on pulse field gradient NMR measurements, raw impedance data and details on analysis of Nyquist plots, temperature dependent ionic and electronic conductivity data, and raw x-ray scattering data.

References

(1) Paulsen, B. D.; Tybrandt, K.; Stavrinidou, E.; Rivnay, J. Organic Mixed Ionic–Electronic Conductors. *Nat. Mater.* **2020**, *19* (1), 13–26.

(2) Rivnay, J.; Inal, S.; Salleo, A.; Owens, R. M.; Berggren, M.; Malliaras, G. G. Organic Electrochemical Transistors. *Nat. Rev. Mater.* **2018**, *3* (17086).

(3) Paulsen, B. D.; Tybrandt, K.; Stavrinidou, E.; Rivnay, J. Organic Mixed Ionic–Electronic Conductors. *Nat. Mater.* **2020**, *19* (1), 13–26.

(4) Son, C. Y.; Wang, Z. G. Ion Transport in Small-Molecule and Polymer Electrolytes. *J. Chem. Phys.* **2020**, *153* (10).

(5) Ratner, M. A.; Shriver, D. F. Ion Transport in Solvent-Free Polymers. *Chem. Rev.* **1988**, *88* (1), 109–124.

(6) Schauser, N. S.; Seshadri, R.; Segalman, R. A. Multivalent Ion Conduction in Solid Polymer Systems. *Mol. Syst. Des. Eng.* **2019**, *4* (2), 263–279.

(7) Noriega, R.; Rivnay, J.; Vandewal, K.; Koch, F. P. V.; Stingelin, N.; Smith, P.; Toney, M. F.; Salleo, A. A General Relationship between Disorder, Aggregation and Charge Transport in Conjugated Polymers. *Nat. Mater.* **2013**, *12* (11), 1038–1044.

(8) Bocharova, V.; Sokolov, A. P. Perspectives for Polymer Electrolytes: A View from Fundamentals of Ionic Conductivity. *Macromolecules* **2020**, *53* (11), 4141–4157.

(9) Ganesan, V. Ion Transport in Polymeric Ionic Liquids: Recent Developments and Open Questions. *Mol. Syst. Des. Eng.* **2019**, *4* (2), 280–293.

(10) Sethuraman, V.; Pryamitsyn, V.; Ganesan, V. Influence of Molecular Weight and Degree of Segregation on Local Segmental Dynamics of Ordered Block Copolymers. *J. Polym. Sci. Part B Polym. Phys.* **2016**, *54* (9), 859–864.

(11) Schauser, N. S.; Grzetic, D. J.; Tabassum, T.; Kliegle, G. A.; Le, M. L.; Susca, E. M.; Antoine, S.; Keller, T. J.; Delaney, K. T.; Han, S.; et al. The Role of Backbone Polarity on Aggregation and Conduction of Ions in Polymer Electrolytes. *J. Am. Chem. Soc.* **2020**, *142* (15), 7055–7065.

(12) Schauser, N. S.; Grzetic, D. J.; Tabassum, T.; Kliegle, G. A.; Le, M. L.; Susca, E. M.; Antoine, S.; Keller, T. J.; Delaney, K. T.; Han, S.; et al. The Role of Backbone Polarity on Aggregation and Conduction of Ions in Polymer Electrolytes. *J. Am. Chem. Soc.* **2020**, *142* (15), 7055–7065.

(13) Schauser, N. S.; Sanoja, G. E.; Bartels, J. M.; Jain, S. K.; Hu, J. G.; Han, S.; Walker, L. M.; Helgeson, M. E.; Seshadri, R.; Segalman, R. A. Decoupling Bulk Mechanics and Mono- and Multivalent Ion Transport in Polymers Based on Metal-Ligand Coordination. *Chem. Mater.* **2018**, *30* (16), 5759–5769.

(14) Sanoja, G. E.; Schauser, N. S.; Bartels, J. M.; Evans, C. M.; Helgeson, M. E.; Seshadri, R.; Segalman, R. A. Ion Transport in Dynamic Polymer Networks Based on Metal-Ligand Coordination: Effect of Cross-Linker Concentration. *Macromolecules* **2018**, *51* (5), 2017–2026.

(15) Buitrago, C. F.; Bolintineanu, D. S.; Seitz, M. E.; Opper, K. L.; Wagener, K. B.; Stevens, M. J.; Frischknecht, A. L.; Winey, K. I. Direct Comparisons of X-Ray Scattering and Atomistic Molecular Dynamics Simulations for Precise Acid Copolymers and Ionomers. *Macromolecules* **2015**, *48* (4), 1210–1220.

(16) Hall, L. M.; Seitz, M. E.; Winey, K. I.; Opper, K. L.; Wagener, K. B.; Stevens, M. J.; Frischknecht, A. L. Ionic Aggregate Structure in Ionomer Melts: Effect of Molecular Architecture on Aggregates and the Ionomer Peak. *J. Am. Chem. Soc.* **2012**, *134* (1), 574–587.

(17) Hall, L. M.; Stevens, M. J.; Frischknecht, A. L. Effect of Polymer Architecture and Ionic Aggregation on the Scattering Peak in Model Ionomers. *Phys. Rev. Lett.* **2011**, *106* (12), 1–4.

(18) Das, P.; Zayat, B.; Wei, Q.; Salamat, C. Z.; Magdău, I.-B.; Elizalde-Segovia, R.; Rawlings, D.; Lee, D.; Pace, G.; Irshad, A.; et al. Dihexyl-Substituted Poly(3,4-Propylenedioxythiophene) as a Dual Ionic and Electronic Conductive Cathode Binder for Lithium-Ion Batteries. *Chem. Mater.* **2020**, *32* (21), 9176–9189.

(19) Lai, C. H.; Ashby, D. S.; Lin, T. C.; Lau, J.; Dawson, A.; Tolbert, S. H.; Dunn, B. S. Application of Poly(3-Hexylthiophene-2,5-Diyl) as a Protective Coating for High Rate Cathode Materials. *Chem. Mater.* **2018**, *30* (8), 2589–2599.

(20) Magdău, I. B.; Miller, T. F. Machine Learning Solvation Environments in Conductive Polymers: Application to ProDOT-2Hex with Solvent Swelling. *Macromolecules* **2021**, *54* (7), 3377–3387.

(21) Webb, M. A.; Savoie, B. M.; Wang, Z. G.; Miller, T. F. Chemically Specific Dynamic Bond Percolation Model for Ion Transport in Polymer Electrolytes. *Macromolecules* **2015**, *48* (19), 7346–7358.

(22) Dokko, K.; Watanabe, D.; Ugata, Y.; Thomas, M. L.; Tsuzuki, S.; Shinoda, W.; Hashimoto, K.; Ueno, K.; Umebayashi, Y.; Watanabe, M. Direct Evidence for Li Ion Hopping Conduction in Highly Concentrated Sulfolane-Based Liquid Electrolytes. *J. Phys. Chem. B* **2018**, *122* (47), 10736–10745.

(23) Bollinger, J. A.; Stevens, M. J.; Frischknecht, A. L. Quantifying Single-Ion Transport in Percolated Ionic Aggregates of Polymer Melts. *ACS Macro Lett.* **2020**, *9* (4), 583–587.

(24) Coropceanu, V.; Cornil, J.; Silva, D.; A, D.; Olivier, Y.; Silbey, R.; Bredas, J. L.; da Silva Filho, D. A.; Brédas, J.-L. J.-L.; Olivier, Y.; et al. Charge Transport in Organic Semiconductors. *Chem. Rev.* **2007**, *107* (4), 926–952.

(25) Mollinger, S. A.; Krajina, B. A.; Noriega, R.; Salleo, A.; Spakowitz, A. J. Percolation, Tie-Molecules, and the Microstructural Determinants of Charge Transport in Semicrystalline Conjugated Polymers. *ACS Macro Lett.* **2015**, *4* (7), 708–712.

(26) Paulsen, B. D.; Frisbie, C. D. Dependence of Conductivity on Charge Density and Electrochemical Potential in Polymer Semiconductors Gated with Ionic Liquids. *J. Phys. Chem. C* **2012**, *116* (4), 3132–3141.

(27) Kunugi, Y.; Harima, Y.; Yamashita, K.; Ohta, N.; Ito, S. Charge Transport in a Regioregular Poly(3-Octylthiophene) Film. *J. Mater. Chem.* **2000**, *10* (12), 2673–2677.

(28) Bridges, C. R.; Ford, M. J.; Thomas, E. M.; Gomez, C.; Bazan, G. C.; Segalman, R. A. Effects of Side Chain Branch Point on Self Assembly, Structure, and Electronic Properties of High Mobility Semiconducting Polymers. *Macromolecules* **2018**, *51* (21), 8597–8604.

(29) Mazaheripour, A.; Thomas, E. M.; Segalman, R. A.; Chabinyc, M. L. Nonaggregating Doped Polymers Based on Poly(3,4-Propylenedioxythiophene). *Macromolecules* **2019**, *52* (5), 2203–2213.

(30) Lim, E.; Glaudell, A. M.; Miller, R.; Chabinyc, M. L. The Role of Ordering on the Thermoelectric Properties of Blends of Regioregular and Regiorandom Poly(3-Hexylthiophene). *Adv. Electron. Mater.* **2019**, *5* (11), 1–11.

(31) Yim, K.-H.; Whiting, G. L.; Murphy, C. E.; Halls, J. J. M.; Burroughes, J. H.; Friend, R. H.; Kim, J.-S. Controlling Electrical Properties of Conjugated Polymers via a Solution-Based p-Type Doping. *Adv. Mater.* **2008**, *20* (17), 3319–3324.

(32) Yamashita, Y.; Tsurumi, J.; Ohno, M.; Fujimoto, R.; Kumagai, S.; Kurosawa, T.; Okamoto, T.; Takeya, J.; Watanabe, S. Efficient Molecular Doping of Polymeric Semiconductors Driven by Anion Exchange. *Nature* **2019**, *572* (7771), 634–638.

(33) Nikolka, M.; Nasrallah, I.; Rose, B.; Ravva, M. K.; Broch, K.; Sadhanala, A.; Harkin, D.; Charmet, J.; Hurhangee, M.; Brown, A.; et al. High Operational and Environmental Stability of

High-Mobility Conjugated Polymer Field-Effect Transistors through the Use of Molecular Additives. *Nat. Mater.* **2017**, *16* (3), 356–362.

(34) Kumar, D.; Sharma, R. C. Advances in Conductive Polymers. *Eur. Polym. J.* **1998**, *34* (8), 1053–1060.

(35) Lazzaroni, R.; Lögdlund, M.; Stafström, S.; Salaneck, W. R.; Brédas, J. L. The Poly-3-Hexylthiophene/NOPF6 System: A Photoelectron Spectroscopy Study of Electronic Structural Changes Induced by the Charge Transfer in the Solid State. *J. Chem. Phys.* **1990**, *93* (6), 4433–4439.

(36) Bubnova, O.; Khan, Z. U.; Wang, H.; Braun, S.; Evans, D. R.; Fabretto, M.; Hojati-Talemi, P.; Dagnelund, D.; Arlin, J.-B.; Geerts, Y. H.; et al. Semi-Metallic Polymers. *Nat. Mater.* **2014**, *13* (2), 190–194.

(37) Köhler, A.; Bässler, H. *Electronic Processes in Organic Semiconductors*; Wiley-VCH Verlag GmbH & Co. KGaA., 2015.

(38) Kivelson, S.; Heeger, A. J. Theory of the Soliton-Lattice to Polaron-Lattice Transition in Conducting Polymers. *Synth. Met.* **1987**, *17* (1–3), 183–188.

(39) Nowak, M. J.; Rughooputh, S. D. D. V. D. V; Hotta, S.; Heeger, A. J. Polarons and Bipolarons on a Conducting Polymer in Solution. *Macromolecules* **1987**, *20* (5), 965–968.

(40) Noriega, R.; Rivnay, J.; Vandewal, K.; Koch, F. P. V.; Stingelin, N.; Smith, P.; Toney, M. F.; Salleo, A. A General Relationship between Disorder, Aggregation and Charge Transport in Conjugated Polymers. *Nat. Mater.* **2013**, *12* (11), 1038–1044.

(41) Spano, F. C.; Silva, C. H- and J-Aggregate Behavior in Polymeric Semiconductors. *Annu. Rev. Phys. Chem.* **2014**, *65* (1), 477–500.

(42) Scholes, D. T.; Yee, P. Y.; Lindemuth, J. R.; Kang, H.; Onorato, J.; Ghosh, R.; Luscombe, C. K.; Spano, F. C.; Tolbert, S. H.; Schwartz, B. J. The Effects of Crystallinity on Charge Transport and the Structure of Sequentially Processed F4TCNQ-Doped Conjugated Polymer Films. *Adv. Funct. Mater.* **2017**, *27* (44), 1–13.

(43) Dong, B. X.; Nowak, C.; Onorato, J. W.; Strzalka, J.; Escobedo, F. A.; Luscombe, C. K.; Nealey, P. F.; Patel, S. N. Influence of Side-Chain Chemistry on Structure and Ionic Conduction Characteristics of Polythiophene Derivatives: A Computational and Experimental Study. *Chem. Mater.* **2019**, *31* (4), 1418–1429.

(44) Giovannitti, A.; Sbircea, D.-T.; Inal, S.; Nielsen, C. B.; Bandiello, E.; Hanifi, D. A.; Sessolo, M.; Malliaras, G. G.; McCulloch, I.; Rivnay, J. Controlling the Mode of Operation of Organic Transistors through Side-Chain Engineering. *Proc. Natl. Acad. Sci.* **2016**, *113* (43), 12017–12022.

(45) Schmode, P.; Ohayon, D.; Reichstein, P. M.; Savva, A.; Inal, S.; Thelakkat, M. High-Performance Organic Electrochemical Transistors Based on Conjugated Polyelectrolyte Copolymers. *Chem. Mater.* **2019**, *31* (14), 5286–5295.

(46) Goel, M.; Thelakkat, M. Polymer Thermoelectrics: Opportunities and Challenges. *Macromolecules* **2020**, *53* (10), 3632–3642.

(47) Schmode, P.; Savva, A.; Kahl, R.; Ohayon, D.; Meichsner, F.; Dolynchuk, O.; Thurn-Albrecht, T.; Inal, S.; Thelakkat, M. The Key Role of Side Chain Linkage in Structure Formation and Mixed Conduction of Ethylene Glycol Substituted Polythiophenes. *ACS Appl. Mater. Interfaces* **2020**, *12* (11), 13029–13039.

(48) Krimalowski, A.; Thelakkat, M. Sequential Co-Click Reactions with Poly(Glycidyl Propargyl Ether) toward Single-Ion Conducting Electrolytes. *Macromolecules* **2019**, acs.macromol.9b00206.

(49) Tang, J.; Chen, Y.; McCuskey, S. R.; Chen, L.; Bazan, G. C.; Liang, Z. Recent Advances in N-Type Thermoelectric Nanocomposites. *Adv. Electron. Mater.* **2019**, *5* (11), 1–15.

(50) Danielsen, S. P. O.; Sanoja, G. E.; McCuskey, S. R.; Hammouda, B.; Bazan, G. C.; Fredrickson, G. H.; Segalman, R. A. Mixed Conductive Soft Solids by Electrostatically Driven Network Formation of a Conjugated Polyelectrolyte. *Chem. Mater.* **2018**, *30* (4), 1417–1426.

(51) Cao, D. X.; Leifert, D.; Brus, V. V.; Wong, M. S.; Phan, H.; Yurash, B.; Koch, N.; Bazan, G. C.; Nguyen, T. Q. The Importance of Sulfonate to the Self-Doping Mechanism of the Water-Soluble Conjugated Polyelectrolyte PCPDTBT-SO3K. *Mater. Chem. Front.* **2020**, *4* (12), 3556–3566.

(52) Bao, Z.; Dodabalapur, A.; Lovinger, A. J. Soluble and Processable Regioregular Poly(3-Hexylthiophene) for Thin Film Field-Effect Transistor Applications with High Mobility. *Appl. Phys. Lett.* **1996**, *69* (26), 4108–4110.

(53) Pipertzis, A.; Mühlinghaus, M.; Mezger, M.; Scherf, U.; Floudas, G. Polymerized Ionic Liquids with Polythiophene Backbones: Self-Assembly, Thermal Properties, and Ion Conduction. *Macromolecules* **2018**, *51* (16), 6440–6450.

(54) Lai, C. H.; Ashby, D. S.; Lin, T. C.; Lau, J.; Dawson, A.; Tolbert, S. H.; Dunn, B. S. Application of Poly(3-Hexylthiophene-2,5-Diyl) as a Protective Coating for High Rate Cathode Materials. *Chem. Mater.* **2018**, *30* (8), 2589–2599.

(55) Patel, S. N.; Javier, A. E.; Stone, G. M.; Mullin, S. A.; Balsara, N. P. Simultaneous Conduction of Electronic Charge and Lithium Ions in Block Copolymers. *ACS Nano* **2012**, *6* (2), 1589–1600.

(56) Patel, S. N.; Javier, A. E.; Balsara, N. P. Electrochemically Oxidized Electronic and Ionic Conducting Nanostructured Block Copolymers for Lithium Battery Electrodes. *ACS Nano* **2013**, *7* (7), 6056–6068.

(57) Javier, A. E.; Patel, S. N.; Hallinan, D. T.; Srinivasan, V.; Balsara, N. P. Simultaneous Electronic and Ionic Conduction in a Block Copolymer: Application in Lithium Battery Electrodes. *Angew. Chemie - Int. Ed.* **2011**, *50* (42), 9848–9851.

(58) Das, B. C.; Szeto, B.; James, D. D.; Wu, Y.; Mccreery, R. L. Ion Transport and Switching Speed in Redox-Gated 3-Terminal Organic Memory Devices. *J. Electrochem. Soc.* **2014**, *161* (12), 831–838.

(59) Pipertzis, A.; Mühlinghaus, M.; Mezger, M.; Scherf, U.; Floudas, G. Polymerized Ionic Liquids with Polythiophene Backbones: Self-Assembly, Thermal Properties, and Ion Conduction. *Macromolecules* **2018**, *51* (16), 6440–6450.

(60) Pipertzis, A.; Papamokos, G.; Mühlinghaus, M.; Mezger, M.; Scherf, U.; Floudas, G. What Determines the Glass Temperature and Dc-Conductivity in Imidazolium-Polymerized Ionic Liquids with a Polythiophene Backbone? *Macromolecules* **2020**, *53* (9), 3535–3550.

(61) Danielsen, S. P. O.; Nguyen, T. Q.; Fredrickson, G. H.; Segalman, R. A. Complexation of a Conjugated Polyelectrolyte and Impact on Optoelectronic Properties. *ACS Macro Lett.* **2019**, *8* (1), 88–94.

(62) Danielsen, S. P. O.; Davidson, E. C.; Fredrickson, G. H.; Segalman, R. A. Absence of Electrostatic Rigidity in Conjugated Polyelectrolytes with Pendant Charges. *ACS Macro Lett.* **2019**, *8* (9), 1147–1152.

(63) Pipertzis, A.; Mühlinghaus, M.; Mezger, M.; Scherf, U.; Floudas, G. Polymerized Ionic Liquids with Polythiophene Backbones: Self-Assembly, Thermal Properties, and Ion Conduction. *Macromolecules* **2018**, *51* (16), 6440–6450.

(64) Scholes, D. T.; Yee, P. Y.; Lindemuth, J. R.; Kang, H.; Onorato, J.; Ghosh, R.; Luscombe, C. K.; Spano, F. C.; Tolbert, S. H.; Schwartz, B. J. The Effects of Crystallinity on Charge Transport and the Structure of Sequentially Processed F4TCNQ-Doped Conjugated Polymer Films. *Adv. Funct. Mater.* **2017**, *27* (44), 1–13.

(65) Bounioux, C.; Díaz-Chao, P.; Campoy-Quiles, M.; Martín-González, M. S.; Goñi, A. R.; Yerushalmi-Rozen, R.; Müller, C. Thermoelectric Composites of Poly(3-Hexylthiophene) and Carbon Nanotubes with a Large Power Factor. *Energy Environ. Sci.* **2013**, *6* (3), 918–925.

(66) Hestand, N. J.; Spano, F. C. Expanded Theory of H- and J-Molecular Aggregates: The Effects of Vibronic Coupling and Intermolecular Charge Transfer. *Chem. Rev.* **2018**, *118* (15), 7069–7163.

(67) Voss, M. G.; Challa, J. R.; Scholes, D. T.; Yee, P. Y.; Wu, E. C.; Liu, X.; Park, S. J.; León Ruiz, O.; Subramaniyan, S.; Chen, M.; et al. Driving Force and Optical Signatures of Bipolaron Formation in Chemically Doped Conjugated Polymers. *Adv. Mater.* **2021**, *33* (3), 1–7.

(68) Lim, E.; Peterson, K. A.; Su, G. M.; Chabinyc, M. L. Thermoelectric Properties of Poly(3-Hexylthiophene) (P3HT) Doped with 2,3,5,6-Tetrafluoro-7,7,8,8-Tetracyanoquinodimethane (F4TCNQ) by Vapor-Phase Infiltration. *Chem. Mater.* **2018**, *30* (3), 998–1010.

(69) Cutler, C. A.; Bouguettaya, M.; Kang, T. S.; Reynolds, J. R. Alkoxysulfonate-Functionalized PEDOT Polyelectrolyte Multilayer Films: Electrochromic and Hole Transport Materials. *Macromolecules* **2005**, *38* (8), 3068–3074.

(70) Merkle, R.; Gutbrod, P.; Reinold, P.; Katzmaier, M.; Tkachov, R.; Maier, J.; Ludwigs, S. Mixed Conductivity of Polythiophene-Based Ionic Polymers under Controlled Conditions. *Polymer (Guildf).* **2017**, *132*, 216–226.

(71) Xia, Y.; Cho, J. H.; Lee, J.; Ruden, P. P.; Frisbie, C. D. Comparison of the Mobility-Carrier Density Relation in Polymer and Single-Crystal Organic Transistors Employing Vacuum and Liquid Gate Dielectrics. *Adv. Mater.* **2009**, *21* (21), 2174–2179.

(72) Kaake, L. G.; Zou, Y.; Panzer, M. J.; Frisbie, C. D.; Zhu, X. Y. Vibrational Spectroscopy Reveals Electrostatic and Electrochemical Doping in Organic Thin Film Transistors Gated with a Polymer Electrolyte Dielectric. *J. Am. Chem. Soc.* **2007**, *129* (25), 7824–7830.

(73) Barteau, K. P.; Wolffs, M.; Lynd, N. A.; Fredrickson, G. H.; Kramer, E. J.; Hawker, C. J. Allyl Glycidyl Ether-Based Polymer Electrolytes for Room Temperature Lithium Batteries. *Macromolecules* **2013**, *46* (22), 8988–8994.

(74) Lascaud, S.; Perrier, M.; Vallée, A.; Besner, S.; Prud'homme, J.; Armand, M. Phase Diagrams and Conductivity Behavior of Poly(Ethylene Oxide)-Molten Salt Rubbery Electrolytes. *Macromolecules* **1994**, *27* (25), 7469–7477.

(75) Snežzana Miljanić, Leo Frkanec, Tomislav Biljan, 3 Zlatko Meić Mladen Žini ć. Recent Advances in Linear and Nonlinear Raman Spectroscopy I. *J. Raman Spectrosc.* **2007**, *38* (April), 1538–1553.

(76) Li, Z.; Smith, G. D.; Bedrov, D. Li+ Solvation and Transport Properties in Ionic Liquid/Lithium Salt Mixtures: A Molecular Dynamics Simulation Study. *J. Phys. Chem. B* **2012**, *116* (42), 12801–12809.

(77) Huang, Q.; Lee, Y. Y.; Gurkan, B. Pyrrolidinium Ionic Liquid Electrolyte with

Bis(Trifluoromethylsulfonyl)Imide and Bis(Fluorosulfonyl)Imide Anions: Lithium Solvation and Mobility, and Performance in Lithium Metal-Lithium Iron Phosphate Batteries. *Ind. Eng. Chem. Res.* **2019**, *58* (50), 22587–22597.

(78) Lassègues, J. C.; Grondin, J.; Talaga, D. Lithium Solvation in Bis(Trifluoromethanesulfonyl)Imide-Based Ionic Liquids. *Phys. Chem. Chem. Phys.* **2006**, 5629–5632.

(79) Dong, B. X.; Nowak, C.; Onorato, J. W.; Strzalka, J.; Escobedo, F. A.; Luscombe, C. K.; Nealey, P. F.; Patel, S. N. Influence of Side-Chain Chemistry on Structure and Ionic Conduction Characteristics of Polythiophene Derivatives: A Computational and Experimental Study. *Chem. Mater.* **2019**, *31* (4), 1418–1429.

(80) Sanoja, G. E.; Schauser, N. S.; Bartels, J. M.; Evans, C. M.; Helgeson, M. E.; Seshadri, R.; Segalman, R. A. Ion Transport in Dynamic Polymer Networks Based on Metal-Ligand Coordination: Effect of Cross-Linker Concentration. *Macromolecules* **2018**, *51* (5), 2017–2026.

(81) Mongcopa, K. I. S.; Tyagi, M.; Mailoa, J. P.; Samsonidze, G.; Kozinsky, B.; Mullin, S. A.; Gribble, D. A.; Watanabe, H.; Balsara, N. P. Relationship between Segmental Dynamics Measured by Quasi-Elastic Neutron Scattering and Conductivity in Polymer Electrolytes. *ACS Macro Lett.* **2018**, *7* (4), 504–508.

(82) Pesko, D. M.; Timachova, K.; Bhattacharya, R.; Smith, M. C.; Villaluenga, I.; Newman, J.; Balsara, N. P. Negative Transference Numbers in Poly(Ethylene Oxide)-Based Electrolytes. *J. Electrochem. Soc.* **2017**, *164* (11), E3569–E3575.

(83) Mongcopa, K. I. S.; Tyagi, M.; Mailoa, J. P.; Samsonidze, G.; Kozinsky, B.; Mullin, S. A.; Gribble, D. A.; Watanabe, H.; Balsara, N. P. Relationship between Segmental Dynamics Measured by Quasi-Elastic Neutron Scattering and Conductivity in Polymer Electrolytes. *ACS Macro Lett.* **2018**, *7* (4), 504–508.

(84) Cheng, Y.; Yang, J.; Hung, J. H.; Patra, T. K.; Simmons, D. S. Design Rules for Highly Conductive Polymeric Ionic Liquids from Molecular Dynamics Simulations. *Macromolecules* **2018**, *51* (17), 6630–6644.

(85) Jorgensen, W. L.; Tirado-Rives, J. Potential Energy Functions for Atomic-Level Simulations of Water and Organic and Biomolecular Systems. *Proc. Natl. Acad. Sci. U. S. A.* **2005**, *102* (19), 6665–6670.

(86) Dodda, L. S.; De Vaca, I. C.; Tirado-Rives, J.; Jorgensen, W. L. LigParGen Web Server: An Automatic OPLS-AA Parameter Generator for Organic Ligands. *Nucleic Acids Res.* **2017**, *45* (W1), W331–W336.

(87) Molinari, N.; Mailoa, J. P.; Kozinsky, B. General Trend of a Negative Li Effective Charge in Ionic Liquid Electrolytes. *J. Phys. Chem. Lett.* **2019**, *10* (10), 2313–2319.

(88) Leontyev, I.; Stuchebrukhov, A. Accounting for Electronic Polarization in Non-Polarizable Force Fields. *Phys. Chem. Chem. Phys.* **2011**, *13* (7), 2613–2626.

(89) Plimpton, S. Short-Range Molecular Dynamics. *J. Comput. Phys.* **1997**, *117* (6), 1–42.

(90) Hockney, R. W.; Eastwood, J. W. *Computer Simulation Using Particles*; CRC Press, 1988.

(91) Danielsen, S. P. O.; Nguyen, T. Q.; Fredrickson, G. H.; Segalman, R. A. Complexation of a Conjugated Polyelectrolyte and Impact on Optoelectronic Properties. *ACS Macro Lett.* **2019**, *8* (1), 88–94.

TOC Graphic

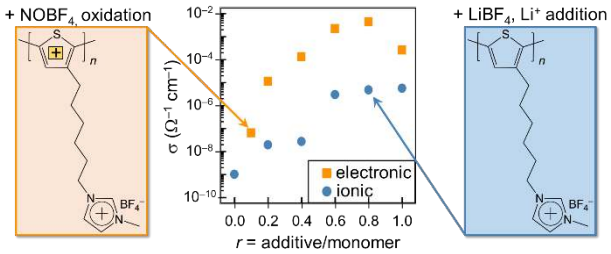
+ NOBF4, oxidation
+ LiBF4, Li+ addition
σ (Ω⁻¹ cm⁻¹)
10⁻²
10⁻⁴
10⁻⁶
10⁻⁸
10⁻¹⁰
electronic
ionic
0.0 0.2 0.4 0.6 0.8 1.0
r = additive/monomer
BF4⁻

Li^+ and Oxidant Addition to Control Ionic and Electronic Conduction in Ionic Liquid Functionalized Conjugated Polymers

Dakota Rawlings,[1] Dongwook Lee,[2] Jeongmin Kim,[4] Ioan-Bogdan Magdău,[4] Gordon Pace,[1] Peter M. Richardson,[2] Elayne M. Thomas,[2] Scott P. O. Danielsen,[1] Sarah H. Tolbert,[5,6] Thomas F. Miller, III,[4] Ram Seshadri,[2,3] Rachel A. Segalman*[1,2]

[1]*Department of Chemical Engineering, University of California, Santa Barbara, Santa Barbara CA 93106, United States*

[2]*Materials Department, University of California, Santa Barbara, Santa Barbara CA 93106, United States*

[3]*Materials Research Laboratory, University of California, Santa Barbara, Santa Barbara CA 93106, United States*

[4]*Division of Chemistry and Chemical Engineering, California Institute of Technology, Pasadena, CA 91125, United States*

[5]*Department of Chemistry and Biochemistry, University of California Los Angeles, Los Angeles CA 90095, United States*

[6]*Department of Materials Science and Engineering, University of California Los Angeles, Los Angeles CA 90095, United States*

To whom correspondence should be addressed: segalman@ucsb.edu

I. Molecular dynamics

Molecular dynamics model. All-atom molecular dynamics simulations were carried out to provide molecular-level mechanistic insights into ion solvation and ion transport. Simulations for P3HT polymers with charged imidazolium side chains were carried out in both crystalline and amorphous phases. Initial configurations of crystalline polymers were generated by stacking 16 straight polymer chains into two separate adjacent stackings (8x2 grid), where each chain consisted of 10 monomers. A BF_4^- counterion was added in the proximity of each imidazolium$^+$ moiety to balance the positive charge. Additionally, an equal number of Li^+ and BF_4^- ions were added in random positions in the simulation box to study the effects of salt concentration. The Li-free polymer (r = 0) was equilibrated for 5 ns. The additional salt was added in gradually, 32 ion pairs at a time (r = 0.2), and at every stage the simulation was equilibrated for an additional 1 ns. Amorphous polymers at each salt concentration were prepared by annealing the crystalline polymers at a higher temperature of 600 K for at least 2 ns, followed by an additional 10 ns equilibration at 400 K.

The OPLS force field,[1] a non-polarizable and all-atom model, was used to describe the potential energy functions of all molecules. Interactions between atoms were described using both electrostatic and Lennard-Jones (LJ) interactions. The cross terms of LJ interaction were obtained using the geometric mixing rule. Intramolecular interactions were described using harmonic potential energy functions for bonds and angles, and the sum of cosine functions for dihedral and improper angles. Bonding and non-bonding coefficients were obtained using the online generator LibParGen.[2] To incorporate the effects of polarizability for ionic species, all atomic charges were multiplied by a constant scalar (0.7) as previously suggested in the MD literature.[3,4] All simulations were conducted using the LAMMPS simulation package.[5]

In all cases during both equilibration and production runs, the MD trajectories were integrated using the velocity-Verlet algorithm with a timestep of 1 fs. Both LJ and Coulomb interactions were cut at 12 Å, and particle-particle particle-mesh Ewald summation[6] was used to compute Coulomb interactions beyond the cutoff distance. Periodic boundary conditions (PBC) were applied for both crystalline and amorphous polymers. The Nosé-Hoover thermostat (100 fs relaxation) and the Nosé-Hoover barostat (1000 fs relaxation) were applied in all simulations to control the temperature (300 K or 400 K) and the pressure (1 atm). All transport properties reported here were averaged using simulation trajectories over at least 80 ns after at least 20 ns long equilibration.

Calculation of Ion-Transport Properties. Charge mean-squared displacement, Σ(t), is calculated via the Einstein relation[7] as follows:

$$\Sigma(t) = \frac{1}{k_B T \langle V \rangle} \sum_{i=1}^{N} \sum_{j=1}^{N} z_i z_j \langle [\vec{r}_i(t) - \vec{r}_i(0)][\vec{r}_j(t) - \vec{r}_j(0)] \delta(|\vec{r}_i(0) - \vec{r}_j(0)| - r_{cut}) \rangle$$

where N is the total number of ions including Li cations, BF_4 anions, and nitrogen atoms of imidazolium pendants, z_i (either +1 e or -1 e) is the charge of i^{th} ion, $\vec{r}_i(t)$ is the position of i^{th} ion at time t, V is the volume of a system, and $\langle \cdots \rangle$ represents the ensemble average. For faster computation, we consider only ion pairs within a cut-off distance, r_{cut} (=8 Å), at an initial time. This Σ(t) is a collective property that takes all correlations into account, whose slope with respect to time is the ionic conductivity. The ion conductivity (σ_{GK}) were estimated using the slope between two points of Σ(t) at t_1=10 ns and t_2=100 ns:

$$\sigma_{GK} = \frac{1}{6} \frac{\Sigma(t2) - \Sigma(t1)}{t2 - t1},$$

where GK represents Green-Kubo formula. Note that in the simulated time window, Σ(t) is not linear with time but sub-diffusive, i.e., Σ(t) ~t^b with an exponent b ≈ 0.8-0.9, indicating that the ionic correlations do not fully decay on timescales less than 100 ns, regardless of salt concentration. Use of different values of time for t_1 and t_2 did not qualitatively change these findings. When all correlations (off-diagonal terms) are negligible, it becomes the same as the Nernst-Einstein (NE) equation:[8]

$$\sigma_{NE} = \frac{e^2}{k_B T \langle V \rangle} N_{monomer} \left[r D_{Li} + (1 + r) D_{BF_4} + D_N \right],$$

where D is ion self-diffusion coefficient (Li, BF_4, or N), $N_{monomer}$ is the total number of monomers, and r is the number ratio of $LiBF_4$ to the monomers. The ion self-diffusion coefficients (D) were estimated using the slope between two points of mean-squared displacement as for σ_{GK}:

$$\mathrm{D} = \frac{1}{6} \frac{MSD(t2) - MSD(t1)}{(t2 - t1)}.$$

Lithium transference number (t_{Li}) is calculated using diffusion coefficients of the ions without taking other correlations into account except for self-correlations[9]: $t_{Li} = tD_{Li}/(D_{Li} + D_{BF_4})$.

Contact duration, *H(t)*, is calculated for a pair of Li and BF_4 as follows:

$$H(t) = \left\langle \frac{h(t)h(0)}{h(0)h(0)} \right\rangle,$$

where *h(t)* = 1 if a pair of Li and BF_4 is within 4 Å at time t, or *h(t)* = 0, otherwise, based on the first plateau in the cumulative distribution of BF_4 around a central Li in Fig. S 5. The average contact duration,

$$\tau = \tau_H \left(\frac{e}{A_H} \right)^{1/b_H},$$

was estimated using a fit to a stretched exponential function: $H(t) \approx A_H \exp[-(t/\tau_H)^{b_H}]$. All the transport coefficients for ionic species in both amorphous and crystalline polymers are given in Table S1 and S2.

Percolating behavior of the ionic network. To quantify the percolation transition of the ionic network as a function of salt concentration, we construct a graph whose nodes are Li ions and B atoms of BF_4 ions. Edges between the nodes are defined if the distance between Li and B is less than 4 Å. We use NetworkX (https://networkx.org) to find the largest cluster in the graph. We define the largest cluster to percolate the simulation box if the longest distance between two Li ions in the cluster is larger than the simulation box size. In this calculation, all the Li ions in the cluster are in the primitive simulation cell, and the longest distance is calculated without periodic boundary conditions applied. Then, the probability of forming a percolating ionic network, P_{perc}, is calculated: $P_{perc} = \langle p \rangle$, where $p = 1$ if the largest cluster percolates the simulation box, or 0 otherwise.

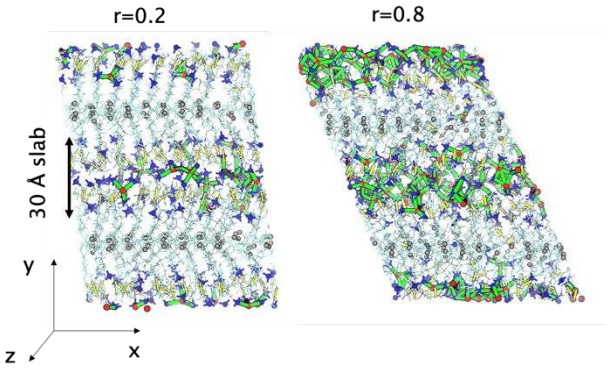

Figure S1: MD snapshots for the crystalline polymers at r=0.2 (left) and r=0.8 (right). The color code is as follows: Red spheres represent Li; blue spheres represent BF4; yellow spheres represent imidazolium nitrogen atoms; grey spheres represent sulfur atoms of thiophene rings; and green lines connect neighboring Li and BF_4 within 4 Å.

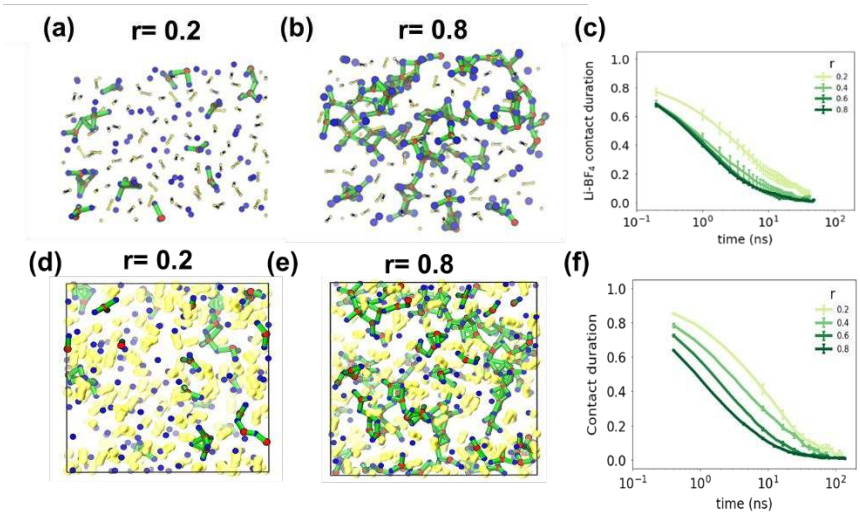

Figure S2: Simulation results for ion solvation and transport in the polymer with added $LiBF_4$ salt. Figures a) through c) show results for the crystalline P3HT-IM polymers at 400 K. Planar view of a 30 Å thin lamellar region at (a) r=0.2 and (b) r=0.8. (c) Li-BF_4 contact duration. The color code for (a) and (b) is as follows: Red spheres represent Li; blue spheres represent BF4; yellow spheres represent imidazolium groups; and green lines connect neighboring Li and BF4 within 4 Å. Figures d) through f) show

simulation results for ion solvation and transport in the amorphous P3HT-IM polymer at 400 K. d) Dispersed localized ion pairs of Li+ and BF4– at low salt concentration (r = 0.2) e) Percolating network of Li+ and BF4– at high salt concentration (r = 0.8). f) Contact duration between Li and BF4– at several salt concentrations.

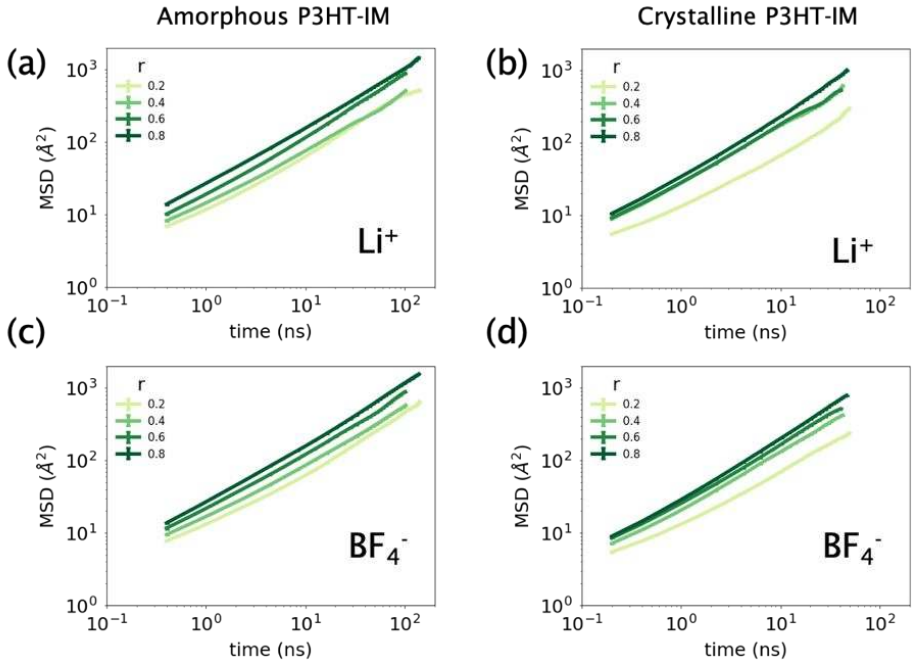

Figure S3: Mean-squared displacement of ions in the amorphous (left column a) and c)) and the crystalline (right column b) and d)) polymers at several salt concentrations.

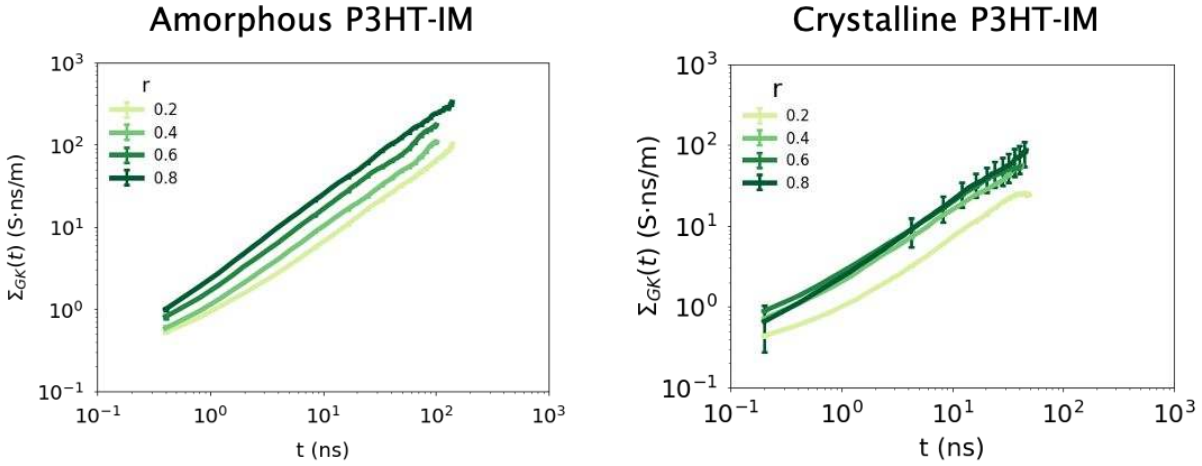

Figure S4: Charge mean-squared displacement, $\Sigma_{GK}(t)$, in the amorphous (left) and the crystalline (right) polymers.

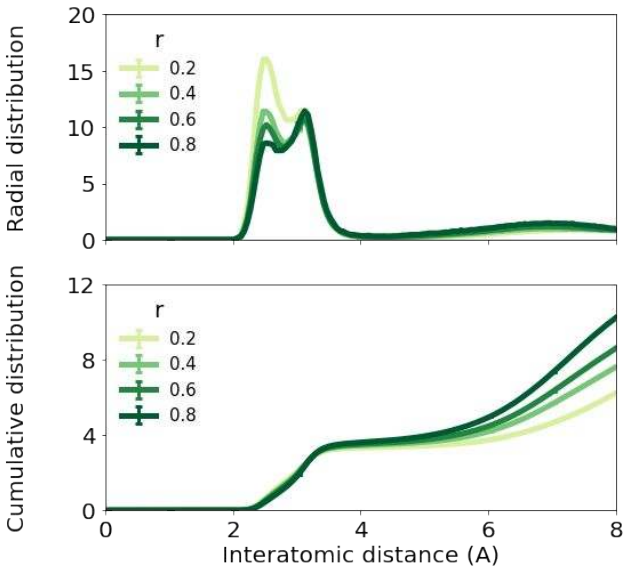

Figure S5: Li solvation by BF_4 in the amorphous polymers as a function of interatomic distance between Li and B.

Table S1: Transport coefficients in the amorphous polymers at 400 K

r ([LiBF$_4$]/[monomer])	τ (ns)	D_{Li} (Å^2/ns)	D_{BF4} (Å^2/ns)	t_{Li}	D_N (Å^2/ns)	σ_{NE} (S/m)	σ_{GK} (S/m)
0.8	1.7 (1)	1.7 (1)	1.8 (1)	0.49	0.09 (1)	0.64 (3)	0.39 (1)
0.6	2.7 (2)	1.4 (1)	1.4 (1)	0.5	0.13 (1)	0.35 (2)	0.28 (1)
0.4	5.9 (5)	0.76 (1)	0.76 (1)	0.5	0.09 (1)	0.25 (2)	0.17 (1)
0.2	10 (2)	0.65 (1)	0.74 (1)	0.47	0.07 (1)	0.09 (1)	0.11 (1)

Table S2: Transport coefficients in the crystalline polymers at 400 K

r ([LiBF$_4$]/[monomer])	τ (ns)	D_{Li} (Å^2/ns)	D_{BF4} (Å^2/ns)	t_{Li}	D_N (Å^2/ns)	σ_{NE} (S/m)	σ_{GK} (S/m)
0.8	1.1 (1)	3.4 (1)	2.6 (2)	0.57	0.07 (1)	0.44 (2)	0.30 (1)
0.6	1.2 (1)	1.7 (1)	1.8 (1)	0.49	0.08 (1)	0.24 (1)	0.26 (1)
0.4	1.8 (2)	1.8 (1)	1.4 (1)	0.56	0.03 (1)	0.17 (1)	0.22 (1)
0.2	4 (1)	0.9 (1)	0.6 (1)	0.6	0.03 (1)	0.08 (1)	0.10 (1)

Solvation environments (SE) of the Li^+ and BF_4^- were studied in the crystalline phase, using the Solvation Environment Classification (SEC) machine learning approach published in our recent work.[10] The molecular environments visited by the ions were characterized using atom-specific cumulative distribution functions (CDFs) calculated with respect to the center of the ion (Li atom for the cation and B atom for the anion). These CDFs (averaged over 10 ps) were concatenated into feature vectors which were embedded in two-dimensional latent space and classified into specific SEs based on the similarity of molecular environments using SEC. Multiple short sample trajectories were used to allow for sufficient sampling of the SEs. The same number of feature vectors ($N_{traj} \times N_{ions} = 9600$) was obtained at each salt concentration by adjusting the number of sampling trajectories to compensate for the varying number of ions. The characterization of SEs resulting from the classification was obtained by inspecting average CDFs, ion binding energy (the non-bonding energy contribution of the force field) and characteristic atomic configurations sampled from each environment (main text).

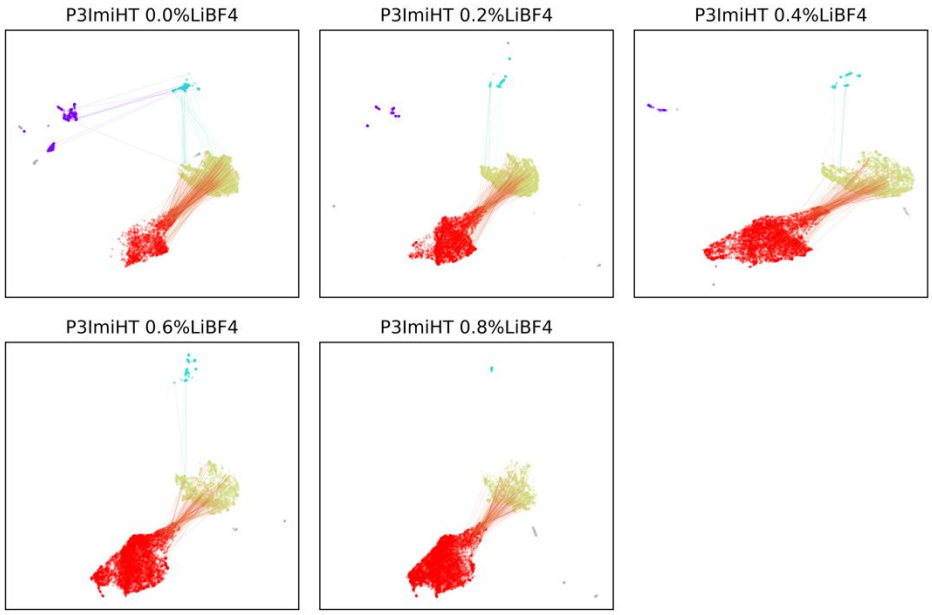

Figure S6: Latent space representation of Li SEs at different salt concentrations.

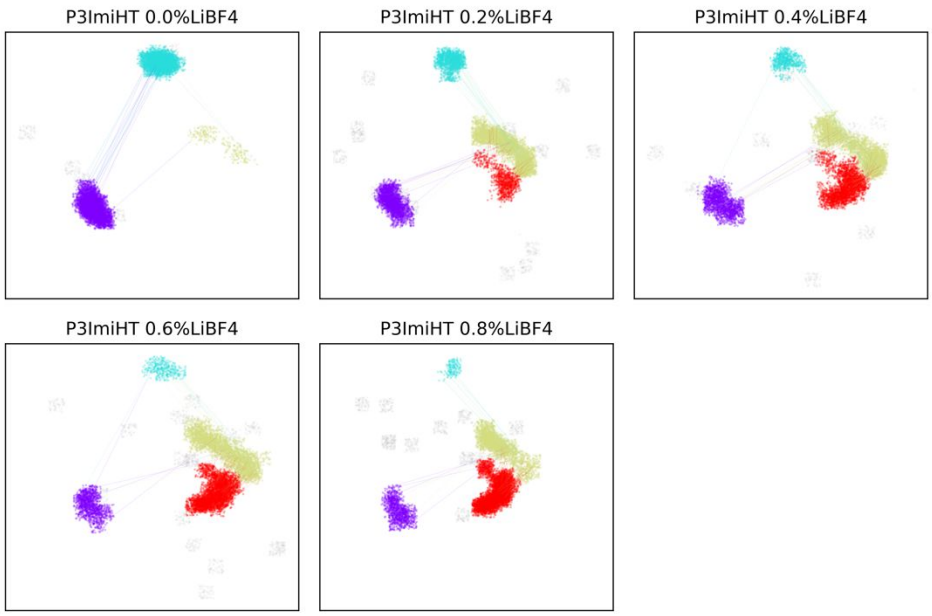

Figure S7: Latent space representation of BF_4 SEs at different salt concentrations.

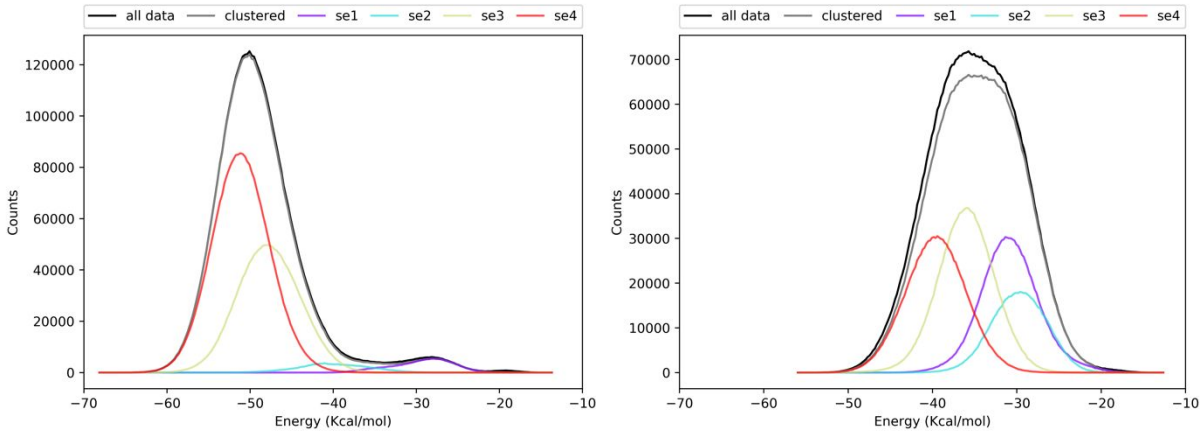

Figure S8: Ion binding energy distribution specific to each SE: Li (left) and BF_4 (right).

Table S3: Calculated $LiBF_4$ concentration and total number of $LiBF_4$ in the simulation for each value of r_{salt}. All simulations were run under constant pressure conditions with a total of 160 monomer units.

		Salt concentration in mol/L		Relative concentration	
r=[salt]/[monomer]	# of LiBF4	amorphous	crystalline	amorphous	crystalline
0.2	32	0.07	0.06	1	1
0.4	64	0.13	0.09	1.9	1.5
0.6	96	0.19	0.12	2.7	2

0.8	128	0.24	0.17	3.6	2

II. Experimental methods

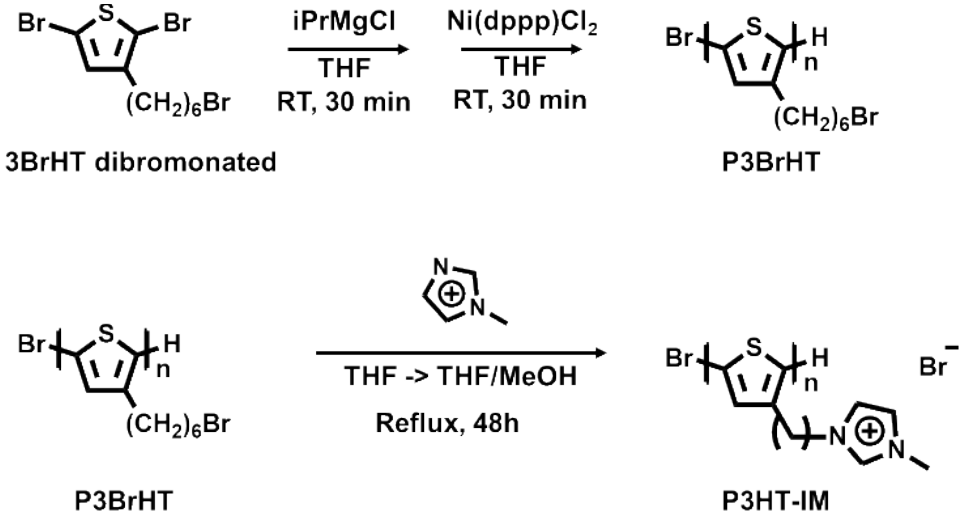

Figure S9: Synthesis of P3BrHT and post-polymerization functionalization to form P3HT-IM Br

Synthesis of Poly[3-(6'-bromohexyl)thiophene] (P3BrHT) Dibromo-3-(6-bromohexyl)thiophene was synthesized according to previous literature.[11,12] An oven-dried Schlenk flask containing 2,5 dibromo-3-(6-bromohexyl)thiophene was placed under vacuum for 2 hours. Dry, degassed THF was added via syringe and the mixture was sparged with Nitrogen. Isopropylmagnesium chloride was added dropwise and the mixture was stirred for 1 h at ambient temperature under Nitrogen. The desired amount of Ni(dppp)Cl2 was added via syringe. The polymerization was stirred for 1 h at 60◦C and quenched by rapid addition of 5 N HCl, and precipitated into methanol. The polymer was purified by washing in a Soxhlet apparatus with methanol, ethyl acetate, and hexanes before extraction with THF. The product was concentrated under vacuum, redissolved in a small amount of THF, and precipitated into rapidly stirring, cold methanol. The isolated product, a purple solid, was dried at 65◦C under vacuum to remove any remaining solvent.
1H NMR (600 MHz, CDCl3) δ 7.18 − 6.92 (m, 1nH), 3.53 − 3.37 (m, 2nH), 2.93 − 2.55 (m, 2nH), 2.04 − 1.81 (m, 2nH), 1.80 − 1.58 (m, 2nH), 1.57 − 1.30 (m, 4nH)
SEC (CHCl3, 35◦C) Mn: 14251 g/mol, Mw: 21086 g/mol, Đ: 1.48

Synthesis of Poly{3-[6'-(N-methylimidazolium)hexyl]thiophene}
The P3BrHT polymer was post-functionalized through an amine quaternization reaction. The polymer was first dissolved in THF. 1 methylimidazole (10 eq.) was added to the solution in ambient conditions. The solution was then stirred for 24 h under reflux. After 12 h, some polymer precipitate was observed int eh flask. A small amount of methanol was added to fully dissolve the resulting polymer and the solution was stirred for an additional 24 hours to help achieve quantitative conversion. The polymers were then dialyzed using 10 kDa cutoff dialysis membranes against a mixture of methanol and THF, with the dialysate replaced every 12 h. The resulting polymer was then mixed with 10 molar equivalents of $LiBF_4$ and stirred at 50°C in methanol and acetonitrile followed by dialysis for 48h in a 50:50 mixture of methanol and acetonitrile and an additional 48h dialysis in acetonitrile. The isolated product was obtained as a red solid after removing

the solvent under reduced pressure. Complete counterion exchange from a bromine counterion to the desired counterion was confirmed using quantitative XPS analysis, following procedures from our previous work.[13] 1H NMR (600 MHz, CD3CN) δ 8.50 (s, 1nH), 7.39-7.34 (m, 2nH), 4.14 (m,2nH), 3.83 (s, 3nH), 2.85 (m, 2H), 1.87 (m, 2nH), 1.71 (m, 2nH), 1.48 (m, 2nH), 1.39 (m, 2nH)

	SampleName	Mn	Mw	Polydispersity
1	DR_P3HT_Br_6_14_19	14251	21086	1.48

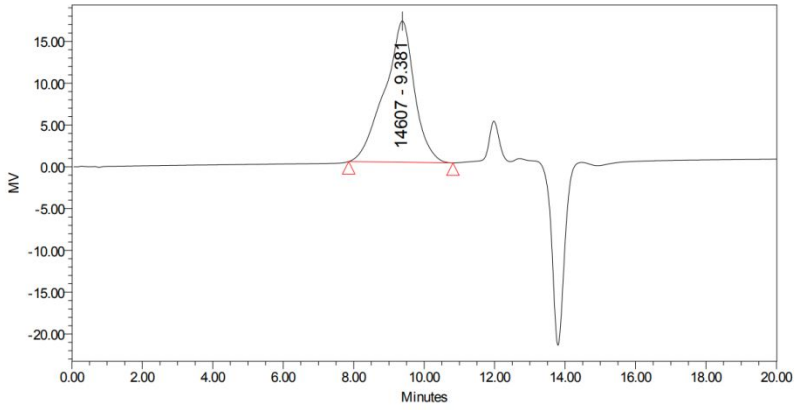

Figure S10: Gel permeation chromatography data for P3BrHT. Molecular weight determination was performed using a polystyrene standard.

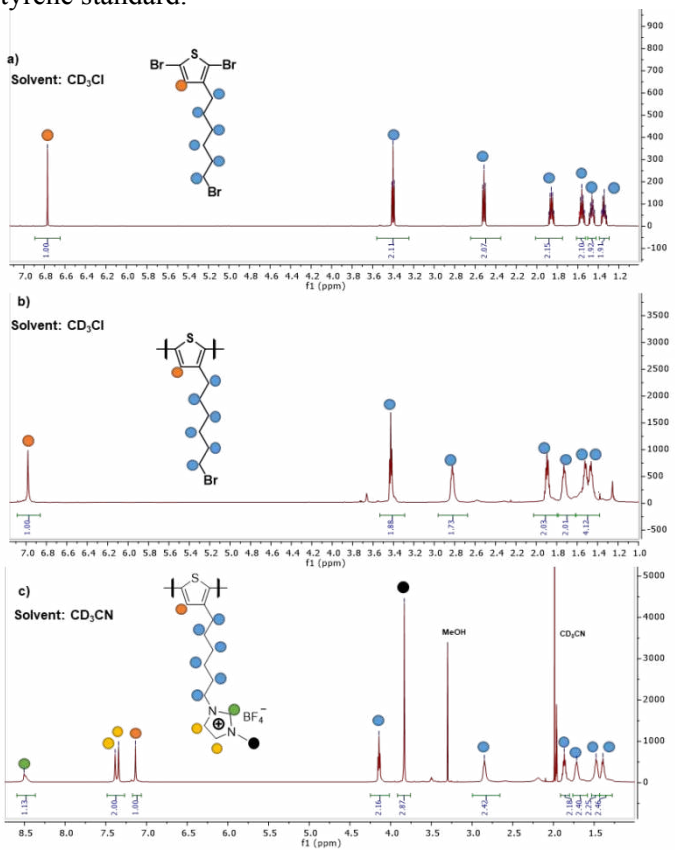

Figure S11: Solution state NMR spectra for a) 3BrHT brominated, b) P3BrHT, and c) P3HT-IM

III. Selection of the optimum counterion for mixed conductivity

UV-vis measurements were performed by spin casting the polymer onto quartz substrates. UV-vis spectra were fit using a model developed by Spano et al[14,15] to determine the 0-0 to 0-1 absorbance ratio.

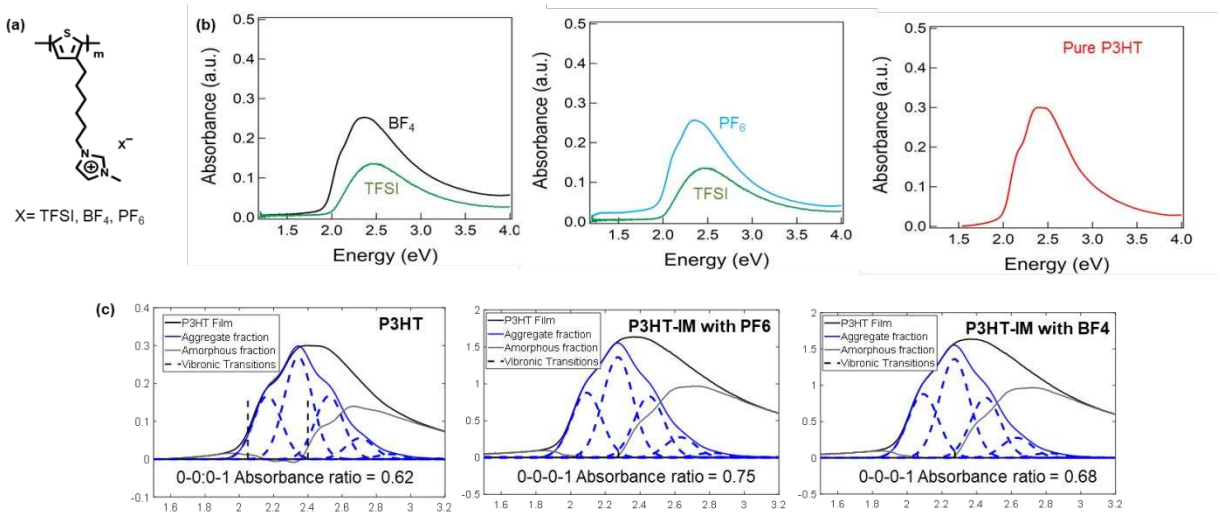

Figure S12: a) Chemical structure of (poly{3-[6′-(N-methylimidazolium)-hexyl]thiophene}, P3HT-IM. b) Optical spectra show the absorbance of P3HT-IM with different counterion species. c) Fit of P3HT spectra. The fitted intensity of the 0-0 and 0-1 transitions were compared for P3HT-IM with different counterions to determine which system had the most ordered aggregate structure

IV. Glass transition measurements via dynamic scanning calorimetry

Polymer samples were cast as described above into standard aluminum pans. The samples were sealed and characterized with a PerkinElmer DSC 8000 to measure the glass transition temperature (T_g) on second heating at 20 °C min^{-1} using the onset method.

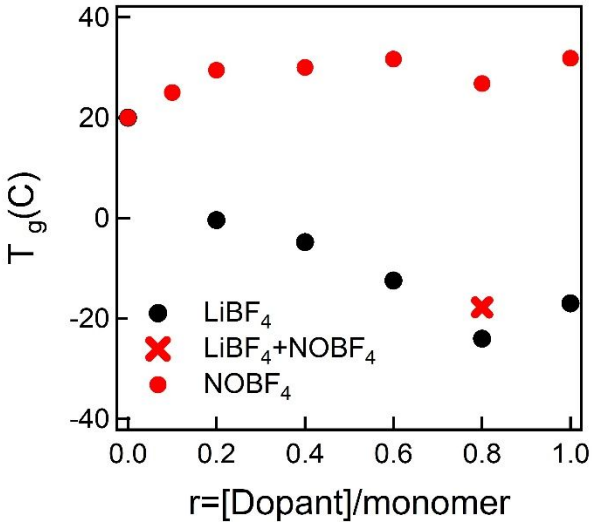

Figure S13: Glass transition temperature of P3HT-IM with both $LiBF_4$ and $NOBF_4$ additives measured via DSC

V. Pulsed Field Gradient NMR measurements

Pulsed Field Gradient (PFG) NMR measures the self-diffusion coefficients of any NMR active nuclei. 7Li and 19F are both NMR active, and correlate to the cation and anion in our system, respectively. Operating under the assumptions of Dilute Solution Theory, the lithium transference number (t_{Li+}) can be calculated, as shown in the following equation

$$t_+ = \frac{D_+}{D_+ + D_-}$$

The PFG NMR sample was prepared at a molar salt concentration of r=1.0 in the same manner as described for the AC Impendence samples. Here, dropcasting was performed into a quartz trough that facilitated approximately 100 mg of material to be loaded into the center of the standard 5mm NMR tube. All sample preparation was done in a nitrogen glovebox, and the NMR tubes were sealed before removal from the glovebox to maintain an oxygen and water free environment during measurement.

Measurements were performed on a 300 MHz Bruker Avance III super-wide-bore spectrometer with a Bruker DIFF50 diffusion probe with replaceable 10 mm radio- frequency (RF) inserts for 7Li and 19F. Due to signal noise and slow diffusion times at room temperature, measurements were performed at 80 C on both ^{19}F and ^{7}Li nuclei. A stimulated echo pulse sequence was used to conserve signal from relatively short T2 values, and the attenuation of the intensity (I) was fit to equation:

$$I(G) = I(0)\exp\left[-G^2 D\,\gamma^2\delta^2\left(\Delta - \frac{\delta}{3}\right)\right]$$

Where G is the magnetic field gradient strength, $I(0)$ is the intensity of the magnetization when G=0, γ is the gyromagnetic ratio, δ is the gradient pulse duration, Δ is the interval between gradient pulses, and D is the self-diffusion coefficient.

Table S4: Experimentally measured diffusion coefficients measured at 80 C using PFG NMR

r ([$LiBF_4$]/[monomer])	D_{Li} ($Å^2$/ns)	D_{BF4} ($Å^2$/ns)	t_{Li}
1.0	0.0145	0.0101	0.59

VI. Impedance Measurements for ionic conductivity

P3HT-IM was prepared by dissolving the polymer in acetonitrile and casting onto a ¼ inch indium tin oxide (ITO) substrate with a circular well in a 150 µm Kapton spacer. $LiBF_4$ salt and $NOBF_4$ were added to the acetonitrile at the specified concentrations prior to casting. The samples were dried under high vac for 24 hours and enclosed with a second ITO substrate. A biologic SP-200 potentiostat was used to perform impedance measurements.

To distinguish the ionic and electronic contributions to the signal, an equivalent circuit was fit to the Nyquist plot which accounts for the ionic resistance, the electronic resistance, and the contact resistance. This was used to determine the ionic conductivity (for electronic conductivity measurements, see section VII). An equivalent circuit consisting of constant phase elements and resistors was utilized. A mixed conducting model circuit was used with a purely resistive component in parallel with an ionic component (a resistor and a constant phase element in series) to account for the electronic and ionic conduction of P3HT-IM. Since the electronic resistance is relatively high for samples with only $LiBF_4$ added, an equivalent circuit without R_e could also be appropriate here. However, we found that the equivalent circuit in **Figure S14** provided a better fit for all data. Furthermore, a pure ion conducting equivalent circuit without the R_e component should give nearly equivalent ionic resistance values compared to the mixed conducting circuit with R_e when the R_e is significantly higher than R_i. From the model circuit in **Figure S14**, the resistance $R_{int\#1}$ at the intercept of the first semicircle with the Z' axis for each Nyquist plot can roughly be expressed as $\frac{1}{R_{int\#1}} = \frac{1}{R_i} + \frac{1}{R_e}$. When the electronic resistance is significantly higher than R_i, the $\frac{1}{R_e}$ term is negligible, and thus the intercept of the first semicircle accurately represents the ionic resistance.

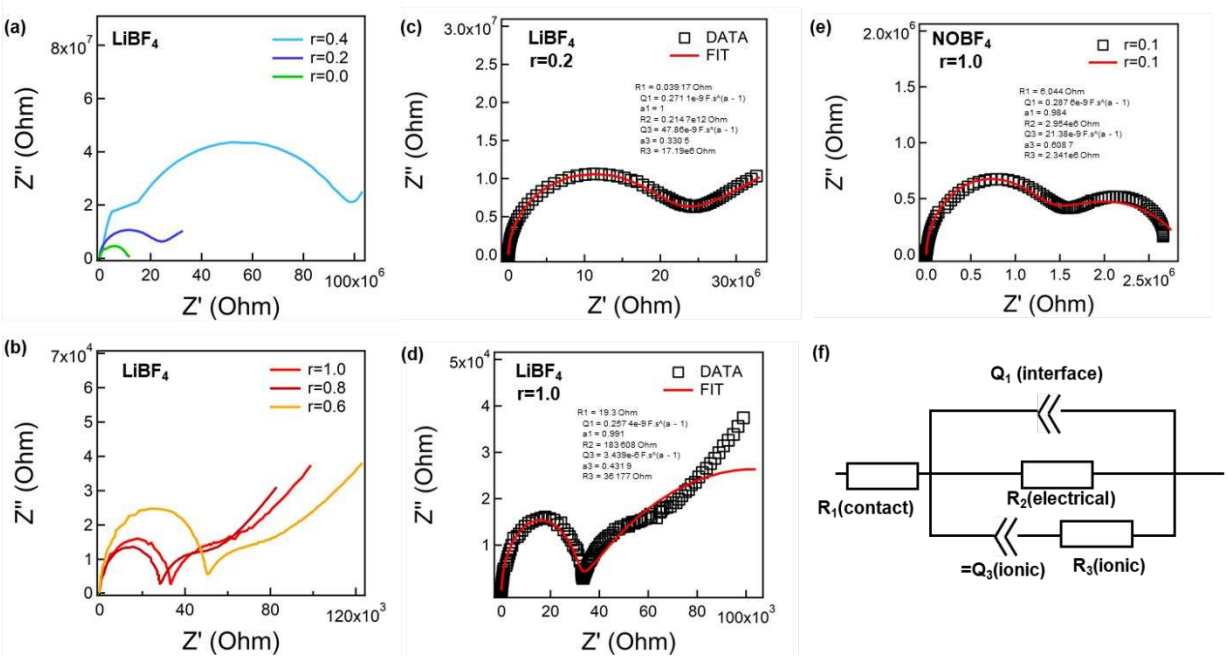

Figure S14: a) and b) Raw Nyquist plots measured for P3HT-IM doped with $LiBF_4$ salt. Example fits of Nyquist plots are shown in c) through e) The equivalent circuit model used to fit the Nyquist plots is shown in f)

VII. Electronic conductivity measurements (DC)

P3HT-IM was prepared for electronic conductivity measurements by dissolving the polymer in acetonitrile and casting onto a ¼ inch indium tin oxide (ITO) substrate with a circular well in a 150 µm Kapton spacer. $LiBF_4$ salt and $NOBF_4$ were added to the acetonitrile at the specified concentrations prior to casting. The samples were dried under high vac for 24 hours and enclosed with a second ITO substrate. A biologic SP-200 potentiostat was used to perform DC conductivity measurements. Here, the voltage was increased in a stepwise manner. The voltage was held for 2.5 minutes at each voltage step to allow the ionic current to relax. This ensured that the measured current was solely from electronic conduction. The plateau current at each voltage value was then plotted vs. voltage (as shown in **Figure S15e**), the slope of the line was used to determine the electronic resistance.

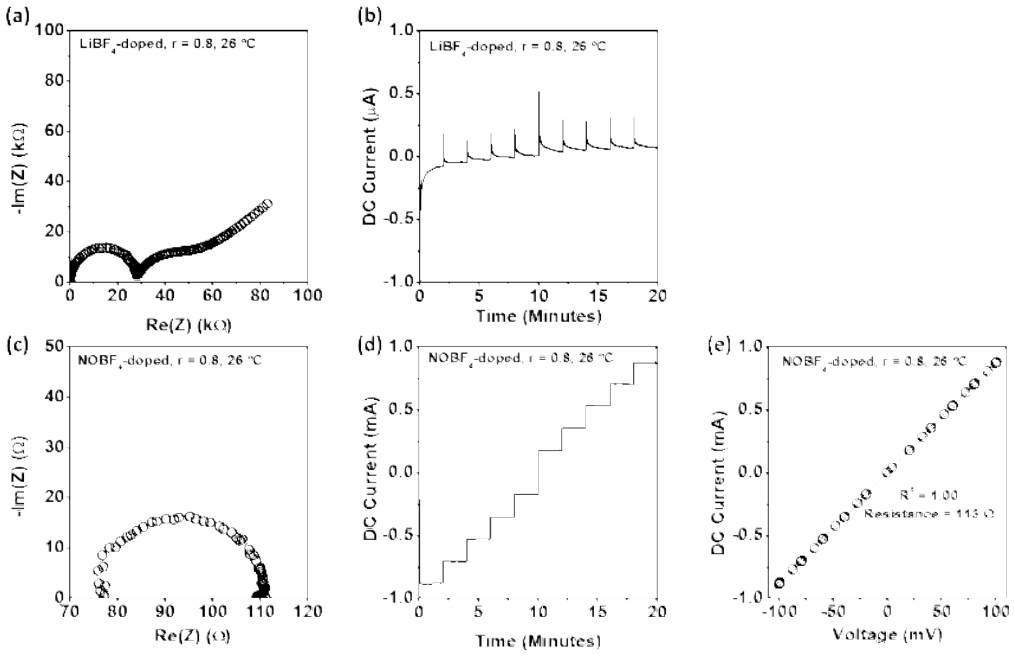

Figure S15: a) Example Nyquist plot measured for $LiBF_4$ salt doped sample at a molar ratio of r=0.8 along with b) DC conductivity measurements used to measure the electric conductivity. c) Example Nyquist plot measured for $NOBF_4$ doped sample at a molar ratio of r=0.8 along with d) and e) the DC conductivity measurement used to determine the electronic conductivity.

VIII. Temperature dependent ionic and electronic conductivity

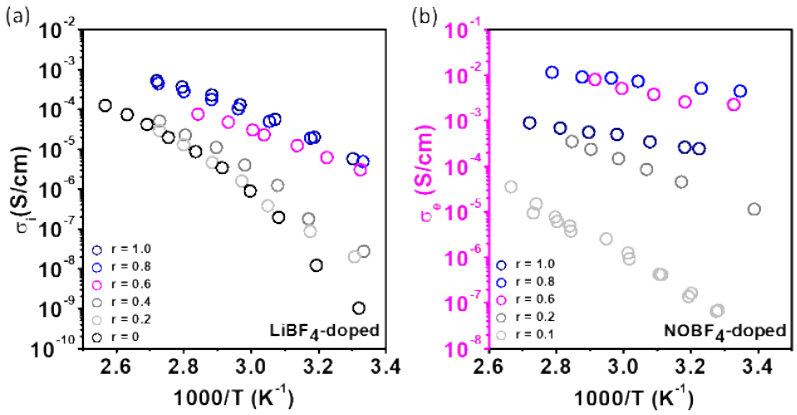

Figure S16: a) Temperature-dependent ionic conductivity for P3HT-IM doped with $LiBF_4$ b) Temperature-dependent electronic conductivity for P3HT-IM doped with $NOBF_4$.

IX. GIWAXS of P3HT-IM with oxidant and salt addition

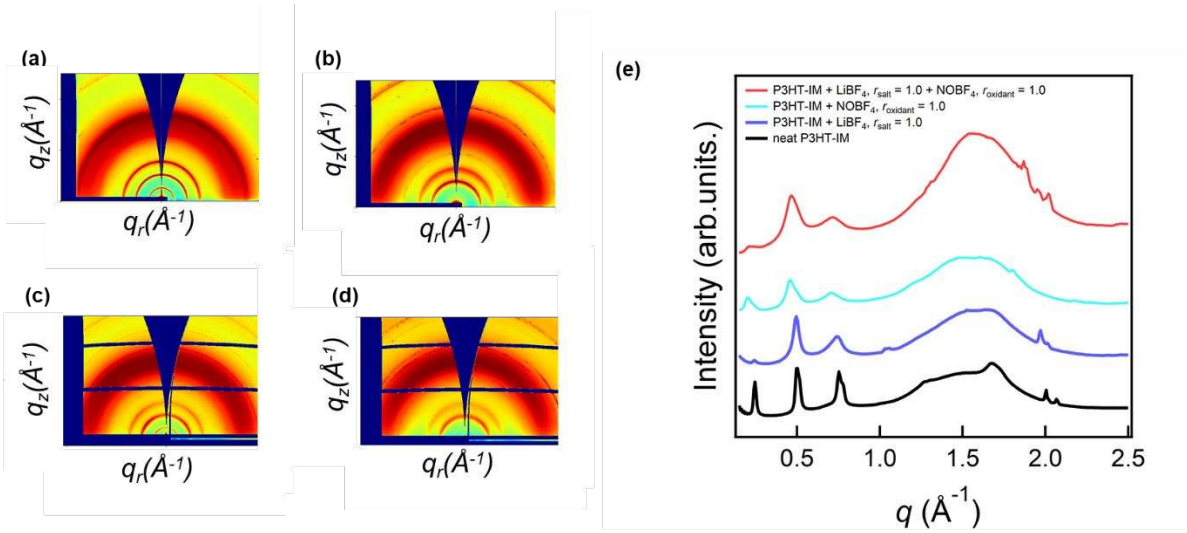

Figure S17: a) GIWAXS pattern for neat P3HT-IM b) GIWAXS pattern for P3HT-IM doped with $LiBF_4$ at a molar ratio of r=1.0. c) GIWAXS pattern for P3HT-IM with $NOBF_4$ d) GIWAXS pattern for P3HT-IM with $NOBF_4$ and $LiBF_4$ e) Integrated GIWAXS patterns for each case

References

(1) Jorgensen, W. L.; Tirado-Rives, J. Potential Energy Functions for Atomic-Level Simulations of Water and Organic and Biomolecular Systems. *Proc. Natl. Acad. Sci. U. S. A.* **2005**, *102* (19), 6665–6670.

(2) Dodda, L. S.; De Vaca, I. C.; Tirado-Rives, J.; Jorgensen, W. L. LigParGen Web Server: An Automatic OPLS-AA Parameter Generator for Organic Ligands. *Nucleic Acids Res.* **2017**, *45* (W1), W331–W336.

(3) Molinari, N.; Mailoa, J. P.; Kozinsky, B. General Trend of a Negative Li Effective Charge in Ionic Liquid Electrolytes. *J. Phys. Chem. Lett.* **2019**, *10* (10), 2313–2319.

(4) Leontyev, I.; Stuchebrukhov, A. Accounting for Electronic Polarization in Non-Polarizable Force Fields. *Phys. Chem. Chem. Phys.* **2011**, *13* (7), 2613–2626.

(5) Plimpton, S. Short-Range Molecular Dynamics. *J. Comput. Phys.* **1997**, *117* (6), 1–42.

(6) Hockney, R. W.; Eastwood, J. W. *Computer Simulation Using Particles*; CRC Press, 1988.

(7) Allen, M. P.; Tildeley, D. J. *Computer Simulation of Liquids*; 2011; Vol. 135.

(8) France-Lanord, A.; Grossman, J. C. Correlations from Ion Pairing and the Nernst-Einstein Equation. *Phys. Rev. Lett.* **2019**, *122* (13), 136001.

(9) Fong, K. D.; Self, J.; McCloskey, B. D.; Persson, K. A. Ion Correlations and Their Impact on Transport in Polymer-Based Electrolytes. *Macromolecules* **2021**.

(10) Magdău, I.-B.; Thomas F. Miller, I. Machine Learning Solvation Environments in Conductive Polymers: Application to ProDOT-2Hex with Solvent Swelling. *Macromolecules* **2021**, *54* (7), 3377–3387.

(11) Danielsen, S. P. O.; Nguyen, T. Q.; Fredrickson, G. H.; Segalman, R. A. Complexation of a Conjugated Polyelectrolyte and Impact on Optoelectronic Properties. *ACS Macro Lett.* **2019**, *8* (1), 88–94.

(12) Danielsen, S. P. O.; Davidson, E. C.; Fredrickson, G. H.; Segalman, R. A. Absence of Electrostatic Rigidity in Conjugated Polyelectrolytes with Pendant Charges. *ACS Macro Lett.* **2019**, *8* (9), 1147–1152.

(13) Danielsen, S. P. O.; Nguyen, T. Q.; Fredrickson, G. H.; Segalman, R. A. Complexation of a Conjugated Polyelectrolyte and Impact on Optoelectronic Properties. *ACS Macro Lett.* **2019**, *8* (1), 88–94.

(14) Spano, F. C.; Silva, C. H- and J-Aggregate Behavior in Polymeric Semiconductors. *Annu. Rev. Phys. Chem.* **2014**, *65* (1), 477–500.

(15) Spano, F. C. Absorption in Regio-Regular Poly(3-Hexyl)Thiophene Thin Films: Fermi Resonances, Interband Coupling and Disorder. *Chem. Phys.* **2006**, *325* (1), 22–35.